Article

Cell Reports

A Circuit for Gradient Climbing in *C. elegans* Chemotaxis

Graphical Abstract

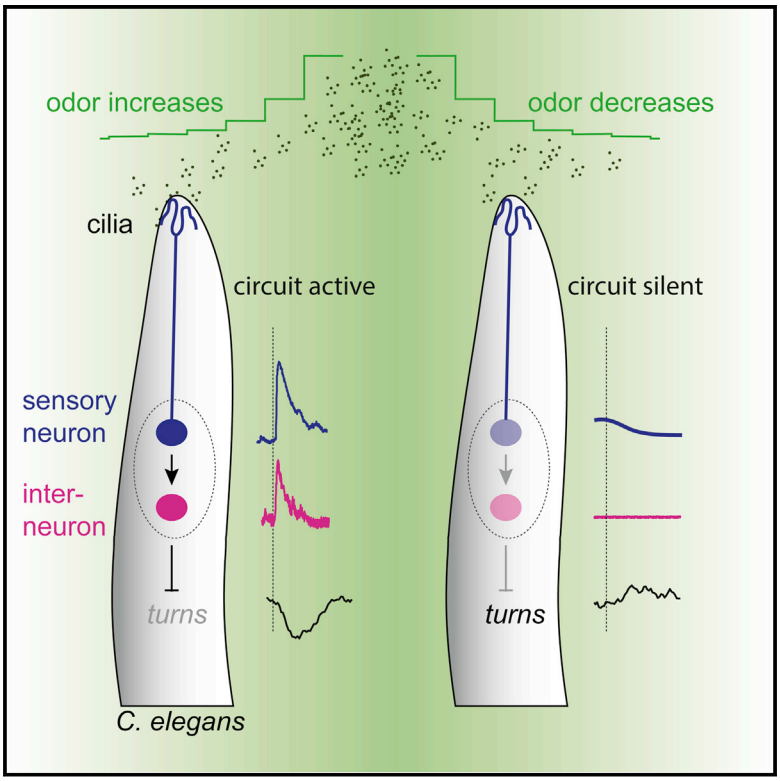

Authors

Johannes Larsch, Steven W. Flavell, Qiang Liu, Andrew Gordus, Dirk R. Albrecht, Cornelia I. Bargmann

Correspondence

cori@rockefeller.edu

In Brief

Sensory systems detect small changes in stimuli across a vast dynamic range. Larsch et al. identify an olfactory circuit in *Caenorhabditis elegans* that reports odor increases over a wide concentration range without saturation. Desensitization and amplification produce a stereotyped, asymmetric neuronal response to odor increases and a matching chemotaxis strategy.

Highlights

- AWA sensory neurons and AIA interneurons are tuned to small odor increases
- AWA has concentration- and history-dependent odor desensitization
- Amplification and desensitization result in a stereotyped AIA response
- AWA desensitization requires intraflagellar transport in cilia

Larsch et al., 2015, Cell Reports *12*, 1748–1760
September 22, 2015
http://dx.doi.org/10.1016/j.celrep.2015.08.032

OPEN ACCESS
CellPress

Cell Reports
Article

A Circuit for Gradient Climbing in *C. elegans* Chemotaxis

Johannes Larsch,[1,2] Steven W. Flavell,[1] Qiang Liu,[1] Andrew Gordus,[1] Dirk R. Albrecht,[1,3] and Cornelia I. Bargmann[1,*]
[1]Howard Hughes Medical Institute, Lulu and Anthony Wang Laboratory of Neural Circuits and Behavior, The Rockefeller University, New York, NY 10065, USA
[2]Present address: Department Genes-Circuits-Behavior, Max Planck Institute of Neurobiology, Am Klopferspitz 18, 82152 Martinsried, Germany
[3]Present address: Department of Biomedical Engineering, Worcester Polytechnic Institute, Worcester, MA 01609, USA
*Correspondence: cori@rockefeller.edu
http://dx.doi.org/10.1016/j.celrep.2015.08.032

SUMMARY

Animals have a remarkable ability to track dynamic sensory information. For example, the nematode *Caenorhabditis elegans* can locate a diacetyl odor source across a 100,000-fold concentration range. Here, we relate neuronal properties, circuit implementation, and behavioral strategies underlying this robust navigation. Diacetyl responses in AWA olfactory neurons are concentration and history dependent; AWA integrates over time at low odor concentrations, but as concentrations rise, it desensitizes rapidly through a process requiring cilia transport. After desensitization, AWA retains sensitivity to small odor increases. The downstream AIA interneuron amplifies weak odor inputs and desensitizes further, resulting in a stereotyped response to odor increases over three orders of magnitude. The AWA-AIA circuit drives asymmetric behavioral responses to odor increases that facilitate gradient climbing. The adaptation-based circuit motif embodied by AWA and AIA shares computational properties with bacterial chemotaxis and the vertebrate retina, each providing a solution for maintaining sensitivity across a dynamic range.

INTRODUCTION

Animals use sophisticated sensory systems and behavioral strategies to navigate to favorable conditions in natural environments. The sensorimotor transformations used in animal navigation provide flexible solutions to unpredictable problems, to the extent that design principles derived from animal navigation have inspired biomimetic engineering of autonomous robots that mimic their spatial computations (Benhamou and Bovet, 1989; Franz and Mallot, 2000). Chemosensory cues—odors and tastes—are produced by all living organisms and provide critical information about nutrients, competitors, mates, and predators. However, they are highly variable in their composition and in their distribution over time and space. Substantial effort has been devoted to understanding the biochemical recognition of odors and tastes by large superfamilies of G-protein-coupled receptors (in mammals and nematodes) and ion channels (in insects) (Bargmann, 2006). Complementary studies have identified higher-order behavioral strategies for tracking odors in gradients (Iino and Yoshida, 2009), in complex plumes (Atema, 1995; Riffell et al., 2008), or across discontinuous boundaries (Vergassola et al., 2007). These two levels of analysis, however, are only incompletely linked to each other by circuits that connect sensory detection with behavioral strategy.

The nematode worm *Caenorhabditis elegans* uses multiple strategies to orient its movement to volatile odors, water-soluble tastes, and temperature. One strategy is a biased random walk reminiscent of bacterial chemotaxis (Berg and Brown, 1972). *C. elegans* locomotion alternates between relatively straightforward runs and sporadic "pirouettes" that change the direction of movement (Pierce-Shimomura et al., 1999). Animals in odor gradients prolong runs when moving toward attractants and increase pirouettes when moving away from the attractants by detecting changes in concentration over time (dC/dt) (Pierce-Shimomura et al., 1999). These behaviors can be recapitulated in response to purely temporal odor pulses in microfluidic environments (Albrecht and Bargmann, 2011). In a second strategy, animals can orient their steering during forward movement to move directly toward an odor source, the "weathervane" behavior (Iino and Yoshida, 2009). Oriented steering appears to result from active sensing in which olfactory signals are temporally coupled with head sweeps during ongoing sinusoidal movement (Izquierdo and Lockery, 2010; Kato et al., 2014).

A challenge for chemotaxis using either strategy is the variation in environmental odor levels experienced as an animal tracks an odor. For example, a point source of the odor diacetyl attracts *C. elegans* over a 100,000-fold concentration range (Bargmann et al., 1993), implying that the underlying sensory systems can maintain sensitivity to odor fluctuations across this range. One mechanism that can prevent saturation at high odor levels is adaptation, a resetting of responsiveness based on sensory history that has been observed in essentially all sensory systems, including bacterial chemosensation (Berg and Brown, 1972), invertebrate and vertebrate olfaction (Reisert and Zhao, 2011; Wilson, 2013), and vision (Montell, 2012; Rieke

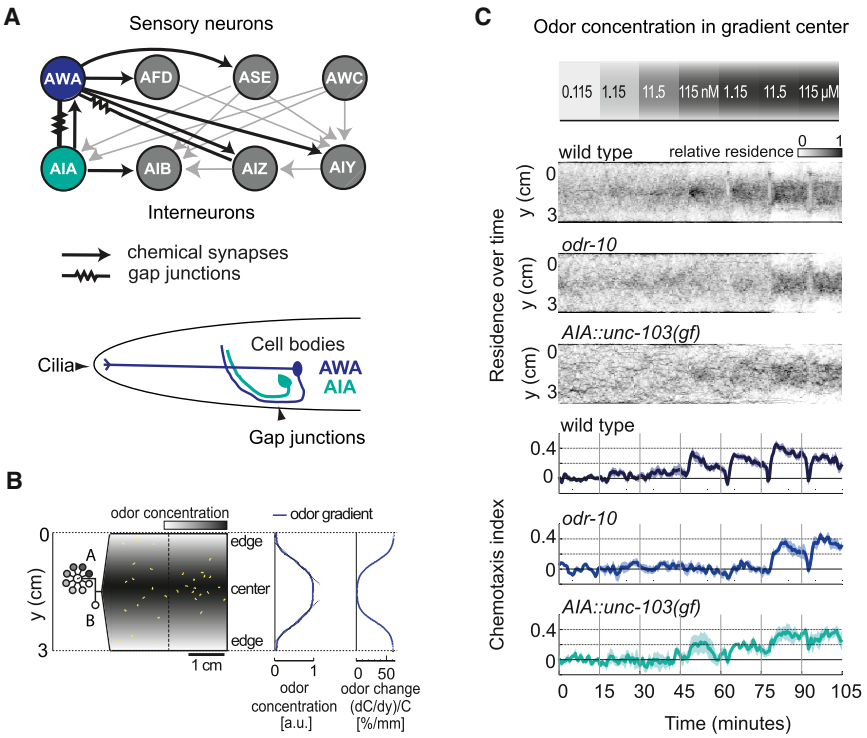

Figure 1. A Neural Circuit for Chemotaxis toward Defined Concentrations of Diacetyl

(A) The AWA circuit. (Top) Part of the *C. elegans* wiring diagram (White et al., 1986), emphasizing synaptic connections between AWA olfactory neurons and other sensory neurons and interneurons. Each sensory neuron has additional targets, and each interneuron integrates input from additional sensory neurons. (Bottom) Schematic illustration of AWA and AIA. AWA detects odors via cilia on the distal sensory dendrite and forms axonal gap junctions with AIA interneurons.

(B) Schematic of microfluidic behavioral device in which sigmoidal odor gradients of known diacetyl concentrations are delivered to freely moving animals. Diacetyl concentrations at the outer edges are held constant at 0.115 nM via inlet B. Peak odor concentration is selected using a computer controlled distribution valve via inlet A. (Middle) Odor concentration profile. Gradient in a.u. scales with peak odor concentration, and the slope of much of the gradient is near linear. (Right) Concentration change per mm experienced by an animal moving toward the center of the arena; animals move at ~0.2 mm/s. See also Movie S1.

(C) Behavior of wild-type and mutant animals in diacetyl gradients. (Top) The peak diacetyl concentration was increased 10-fold as indicated every 15 min. (Middle three panels) Distribution of animals in the device expressed as a density function of residence over time. (Bottom three panels) A mean chemotaxis index represented the location of animals in the device during 2-s time bins (continuous scale from −1 at device edge to +1 at device center). *odr-10(ky32)* mutants lack the AWA diacetyl receptor. *unc-103(gf)* strains express a hyperactive K+ channel in the AIA neurons under the *gcy-28d* promoter. Shading represents SEM. n = 4–6 assays with 20–30 animals per genotype.

and Rudd, 2009). In addition to extending the dynamic range of the system, adaptation tunes it to changes in stimulus intensity in preference to absolute stimulus levels, a feature that would promote both biased random walk and steering behavior.

In *C. elegans,* two pairs of ciliated chemosensory neurons called AWA and AWC mediate attraction to volatile odors. Chemotaxis to low concentrations of diacetyl requires the AWA sensory neurons and ODR-10, a G-protein-coupled olfactory receptor (Bargmann et al., 1993; Sengupta et al., 1996). Other GPCRs in AWA and AWC are thought to detect other odors. AWA calcium levels increase upon odor addition, suggesting depolarization (Larsch et al., 2013; Shinkai et al., 2011), whereas AWC calcium levels decrease in odor, suggesting hyperpolarization (Chalasani et al., 2007). AWA and AWC have distinct but overlapping synaptic partners: for example AWA forms gap junctions onto AIA interneurons, whereas AWC forms chemical synapses onto AIA (Figure 1A). These observations suggest that AWA and AWC perform functionally distinct computations, even though they both give rise to odor chemotaxis behavior.

Multiple interneurons, including AIA, AIB, and AIY, are regulated by the odors sensed by AWA and AWC and may therefore provide the neuronal substrates that link sensory detection to a behavioral response. The integrating interneurons downstream of AWA and AWC are functionally redundant for chemotaxis in a general sense, but quantitative assays indicate that they have distinguishable functions. For example, AIB interneurons set reversal rates in the biased random-walk strategy (Iino and Yoshida, 2009; Luo et al., 2014), and AIY interneurons are required for steering (Satoh et al., 2014), but neither AIB nor AIY is essential for chemotaxis in odor gradients. In this work, we implicate another interneuron, AIA, in the dynamic detection of odor increases and define the algorithm by which it contributes to chemotaxis behavior.

Establishing the precise relationships among odor distribution, neuronal recruitment and dynamics, and resulting chemotaxis behaviors is challenging. The development of high-throughput, quantitative methods for monitoring neuronal calcium signaling and behavior in *C. elegans* in well-controlled environments provides the opportunity to analyze these features of chemosensory circuits (Albrecht and Bargmann, 2011; Larsch et al., 2013). Here, we define properties of AWA sensory neurons and AIA integrating interneurons that allow them to represent a wide range of odor concentrations and concentration changes. We show that these neurons are dynamically tuned to detect odor increases, enabling them to drive a specialized, asymmetric strategy for gradient climbing in chemotaxis.

RESULTS

AWA Calcium Dynamics Are Shaped by Odor History on Multiple Timescales

The AWA sensory neuron is essential for chemotaxis to diluted diacetyl on agar plates, but the odor concentrations that the animal experiences in these assays are unknown. To define the relationship between chemotaxis and concentration, we monitored the behavior of *C. elegans* in microfluidic arenas while

delivering precise spatial and temporal patterns of diacetyl odor in an all-liquid environment (Albrecht and Bargmann, 2011) (Figure 1B; Movie S1). Chemotaxis to diacetyl was assayed in sigmoidal odor gradients in which animals controlled their own sensory experience by moving in the gradient, as they do during chemotaxis on agar plates. Wild-type animals preferentially migrated toward peak diacetyl concentrations from 11 nM to 115 μM, showing peak accumulation within 5 minutes and then dispersing slightly over the following 10 minutes (Figure 1C; for simplicity, approximate odor concentrations will be used in the text). Mutant animals lacking the AWA diacetyl receptor ODR-10 did not chemotax when the peak diacetyl concentration was below 10 μM, indicating that ODR-10 and by implication AWA are required for chemotaxis in the nanomolar to low-micromolar range (Figure 1C). AWA forms synapses with multiple sensory neurons and interneurons, including AIA (Figure 1A). When AIA interneurons were silenced by expression of the leaky potassium channel *unc-103(gf)* (Petersen et al., 2004), chemotaxis to diacetyl was less precise (Figure 1C). The contribution of AIA to AWA-dependent behavior is considered further below.

To relate neuronal responses to behavior, a similar microfluidic device was used to monitor odor-evoked neuronal activity in animals expressing genetically encoded calcium indicators in the GCaMP series (Akerboom et al., 2012; Larsch et al., 2013; Tian et al., 2009) (Figure 2A). Diacetyl pulses from 1 nM to 100 μM elicited transient, dose-dependent calcium increases in AWA sensory neurons that were strongly dependent on odor concentration and stimulus duration (Figure 2B). Reponses to a 30-s pulse of 1–10 nM diacetyl were weak but persisted through the stimulus; responses to 100 nM to 10 μM diacetyl peaked within 10 s and then decreased during stimulation; responses to 100 μM diacetyl did not decrease. These concentration- and history-dependent AWA decreases are defined as desensitization. Desensitization had characteristic rates at each concentration (Figure 2C) and was incomplete. For example, at 1 μM diacetyl, AWA calcium fell in 1 min to a low steady-state level that was maintained for at least 5 min (Figure 2D). Thus, the AWA response to behaviorally relevant diacetyl concentrations includes a strongly desensitizing range.

When 30-s pulses were delivered once per minute, AWA responses fell in each successive trial, an effect that was strongest at 100 nM (Figures 2E and 2F). This decrease between trials, defined as habituation, was observed even for low diacetyl concentrations that did not desensitize within a trial. Habituation rescaled response magnitude but largely preserved the desensitization characteristics of each odor concentration (Figures 2E and 2F). Habituation was strong across the first few trials but diminished thereafter. For example, in a 5-hr experiment in which animals were pulsed once per minute with 1 μM diacetyl for 5 s, the magnitude of AWA calcium responses fell rapidly during the first seven odor pulses, then slowly over the next ~300 pulses (Figure 2g). Other odor stimuli and patterns showed the same two phases of AWA habituation (data not shown).

In combination, these experiments demonstrate effects of odor history on AWA calcium responses at multiple timescales: rapid concentration-dependent desensitization that begins within a few seconds of odor onset and at least two forms of habituation with different kinetics.

The Relationship between Voltage, Calcium, and GCaMP Responses in AWA Neurons

A variety of biochemical processes fall between diacetyl detection and GCaMP signals in AWA neurons: the activation of the ODR-10 receptor and subsequent G protein pathways, depolarization and calcium entry through the transient receptor potential vanilloid (TRPV) sensory transduction channel, signal amplification through voltage-gated calcium channels in the cell body, calcium extrusion, and calcium-to-fluorescence conversion by GCaMP. In principle, any of these processes could change during AWA desensitization.

To distinguish whether desensitization occurs upstream and downstream of voltage changes, we used the red-shifted Chrimson variant of channelrhodopsin (Klapoetke et al., 2014) to directly depolarize AWA while recording calcium signals with GCaMP2.2b (Figure 3A). Electrophysiological recordings of Chrimson-expressing AWA neurons under current clamp demonstrated that red light induced rapid depolarization that was stable during a 10- or 30-s stimulation and quickly returned to the resting membrane potential after light shutoff (Figure 3B). Chrimson activation with red light also induced saturable GCaMP calcium increases in AWA, with a similar peak magnitude as those induced by odor (Figure 3C). This depolarization-induced fluorescence rose with a $t_{1/2}$ of 1 s, desensitized during sustained illumination with a $t_{1/2}$ of 25 s, and decayed after the end of the stimulus with a $t_{1/2}$ of 5 s (Figures 3C–3E and S3).

Odor concentrations above 100 nM resulted in AWA calcium increases with a rapid rise time consistent with depolarization (Figures 3C and S3). Odor removal led to a decay in calcium signals with a $t_{1/2}$ of 5 s, the same as observed at the end of Chrimson illumination (Figures 3D and 3E). Identical rates of post-odor fluorescence decay were observed across different odor concentrations, durations of odor exposure, and calcium levels (Figures 3D and S3). These results indicate that odor removal and Chrimson shutoff are equivalent with respect to this sensor and suggest that odor removal triggers a voltage decrease in AWA followed by a fixed rate of calcium efflux.

In the presence of sustained odor, however, AWA responded differently than under sustained Chrimson illumination. Near 1 μM diacetyl, calcium fell with a $t_{1/2}$ of 7.5 s, almost as quickly as when odor was removed. A similar rapid calcium decay was observed with 100 nM odor, but not at higher or lower concentrations, even when peak signals were the same (e.g., 1 and 10 μM odor) (Figures 2 and 3). The distinct decay patterns with Chrimson and different odor concentrations suggest that desensitization cannot be explained purely by uncoupling calcium from voltage or by increased calcium efflux. A consistent single explanation for these results is that AWA desensitizes to intermediate odor concentrations at a step in olfactory transduction before cell-body depolarization. The AWA responses to odor and Chrimson began to diverge within the first second of the calcium trace, suggesting that desensitization is initiated within this time.

By testing different calcium sensors and conditions, we considered how technical properties of GCaMPs and reporter strains limit the sensitivity and time resolution of these experiments (Figure S1). Desensitization to intermediate odor concentrations was robust and observed with all sensors.

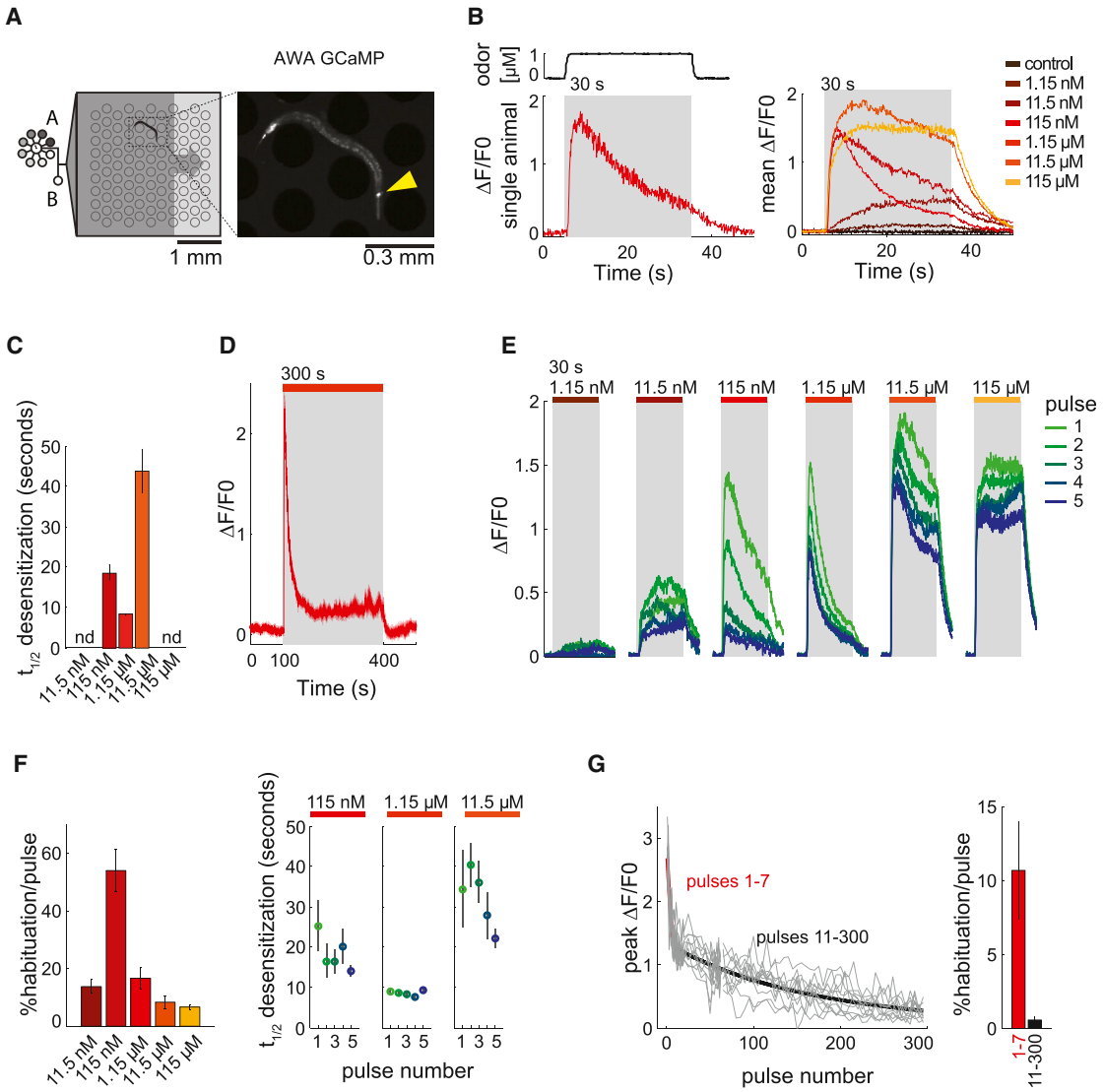

Figure 2. AWA Calcium Dynamics Are Shaped by Odor Concentration and History

(A) Schematic of a 3 × 3-mm microfluidic imaging device, illustrating flow of odor past animals in a pulse assay, and a camera frame showing GCaMP2.2b fluorescence in an AWA sensory neuron (arrowhead).

(B) AWA calcium response to 30-s pulses of diacetyl. (Top left) Odor switches from 10% to 90% final concentration within 1 s, based on dye measurement. (Bottom left) Single trace at 1.15 μM. (Right) Average of multiple trials; n = 9 animals, five pulses at each concentration.

(C) AWA desensitization rates within 30-s odor pulses (data from B). nd, not detectable.

(D) AWA calcium response to a 5-min pulse of 1.15 μM diacetyl; trace shading represents SEM. n = 12 animals, 1 trial each.

(E) AWA calcium responses to five successive 30-s pulses of odor at each concentration. Green, first pulse; blue, last pulse. n = 9 animals tested across all concentrations.

(F) (Left) Habituation of peak AWA fluorescence between pulses. (Right) Desensitization rates within pulses, with repeated pulses at the same concentration. Error bars represent SEM. n = 9 animals.

(G) Peak AWA fluorescence to 5-s pulses of 1.15 μM diacetyl delivered once every 60 s. Gray, 11 individual animals; red and black, best fit to the equation $y(t) = y_0 * \exp(-k*t)$ separately during two phases: (1) pulses 1–7 and (2) pulses 11–300. Habituation rate k represents decrease of peak AWA fluorescence per 5-s pulse. Error bars represent SEM. n = 11 animals.

Intraflagellar Transport Proteins and Inositol Phospholipids Regulate AWA Desensitization and Habituation

To define the molecular requirements for AWA odor detection and desensitization, mutant strains were examined, beginning with genes that affect sensory transduction (Figures 4A and S2). AWA calcium transients in *odr-10* mutants were reduced >1,000-fold in sensitivity, confirming ODR-10 as the primary AWA diacetyl receptor (Figures 4A and S2). Calcium responses were absent in *osm-9* and *ocr-1 ocr-2* mutant animals, which

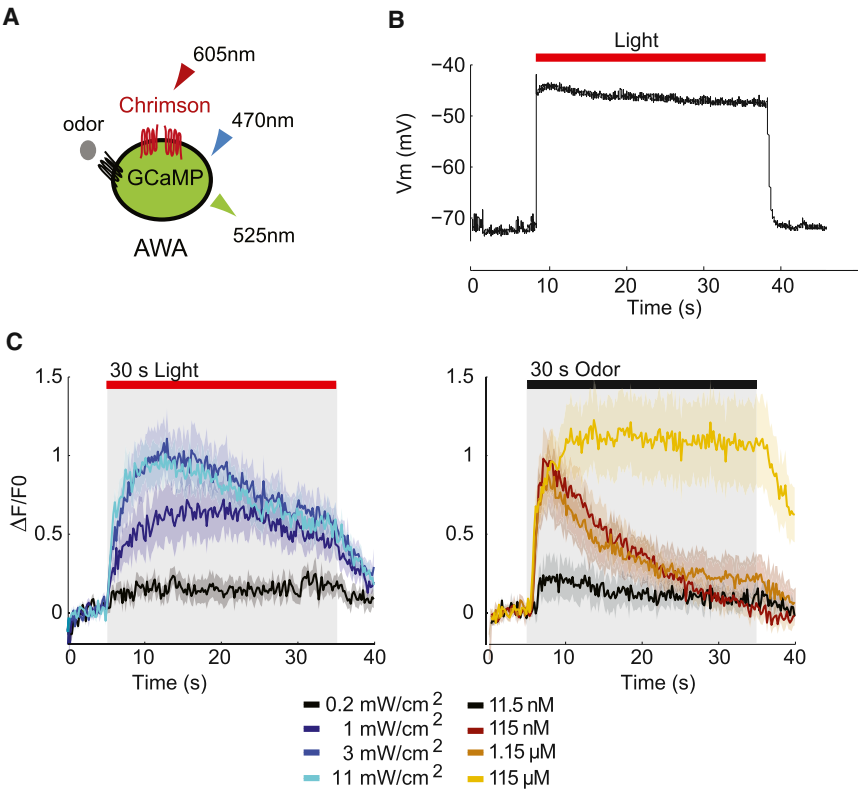

Figure 3. Contribution of Voltage to GCaMP Dynamics

(A) Coexpression of the red-shifted Chrimson cation channel with GCaMP2.2b in AWA. Red light excites Chrimson to depolarize AWA; blue light excites GCaMP2.2b in AWA.

(B) Electrophysiological responses of AWA neuron to depolarization by Chrimson. Representative trace in current clamp during 30 s of illumination; n = 7 traces.

(C) (Left) AWA calcium response during Chrimson stimulation for 30 s at different light intensities. (Right) AWA calcium response during odor stimulation of the same animals. Shading represents SEM. Note that desensitization results in a faster time to peak, a typical feature of sensory systems. n = 10 animals.

(D) Decay of AWA GCaMP fluorescence after Chrimson illumination and after removal of a 30-s or 10-s odor stimulus. Colors indicate stimuli as in (C). Inset: normalized fluorescence after 10 s odor stimuli, time shifted to illustrate similar rates of decay. Data from 10 s odor are in Figure 4A.

(E) Rates of desensitization in continuous light (Chrimson) or continuous odor from (C). For other odor stimuli, see Figure 2. For additional GCaMP indicators and further discussion of calcium signaling dynamics, see Figure S1.

disrupt the TRPV transduction channels, and reduced 1,000-fold in sensitivity in *ocr-2* single mutants (Figure 4A). AWA calcium responses were strongly reduced in the L-type voltage-gated calcium channel mutant *egl-19(n582),* suggesting that a voltage-to-calcium transformation is essential to the AWA calcium signal.

AWA odor responses, desensitization, and habituation were all normal in mutants for the arrestin homolog *arr-1*, suggesting that arrestin modulation of GPCR signaling is not central to response regulation (Figure S2). Similarly, AWA odor responses were unchanged in the synaptic transmission-defective mutants *unc-18(e234), unc-13(e51)* and *unc-13(s69)* (Richmond et al., 1999; Weimer et al., 2003), suggesting that diacetyl detection, desensitization, and habituation are largely independent of fast synaptic input (Figure S2). A small enhancement of habituation and desensitization was observed in the neuropeptide release-defective mutant *unc-31* and the neuropeptide processing mutant *egl-3,* suggesting a minor role of neuropeptide signaling in response regulation (Figure S2).

We fortuitously discovered a role for intraflagellar transport (IFT) proteins in sensory regulation through studies of the strain CB450, which bears an *unc-13(e450)* mutation and did not show fast desensitization at any odor concentration (Figures 4A and S2). High-throughput imaging, linkage analysis, and whole-genome sequencing demonstrated that the defect was not caused by the *unc-13* mutation but rather by a linked mutation in *che-3*, which encodes a ciliary dynein heavy-chain motor protein that regulates cilium structure (Wicks et al., 2000). Three other IFT mutants, *che-3(e1124)*, *osm-6(p811)*, and *che-2(e1033)*, also failed to desensitize or habituate to diacetyl (Figures 4A, 4B, S2, and S3).

IFT mutations decrease sensory responses in most ciliated sensory neurons (Inglis et al., 2007), but AWA had robust calcium responses across a range of odor concentrations in *che-2*, *che-3*, and *osm-6* mutants (Figures 4A and 4B) and only mild defects in diacetyl chemotaxis at the concentrations at which AWA is required (Bargmann et al., 1993; Matsuura et al., 2013; Figure S3). All of the IFT mutants had abnormal AWA cilia, in agreement with previous studies (Figures 4C and S3 and data not shown). The defect in *osm-6(p811)* was rescued by AWA-restricted expression of an *osm-6* cDNA (Figure 4A). These results indicate that IFT plays a direct or indirect role in AWA desensitization and habituation.

A defect in AWA dynamics reciprocal to that of the IFT mutants was present in a previously uncharacterized chemotaxis-defective mutant, *ky121* (Roayaie, 1996). *ky121* mutants had diminished

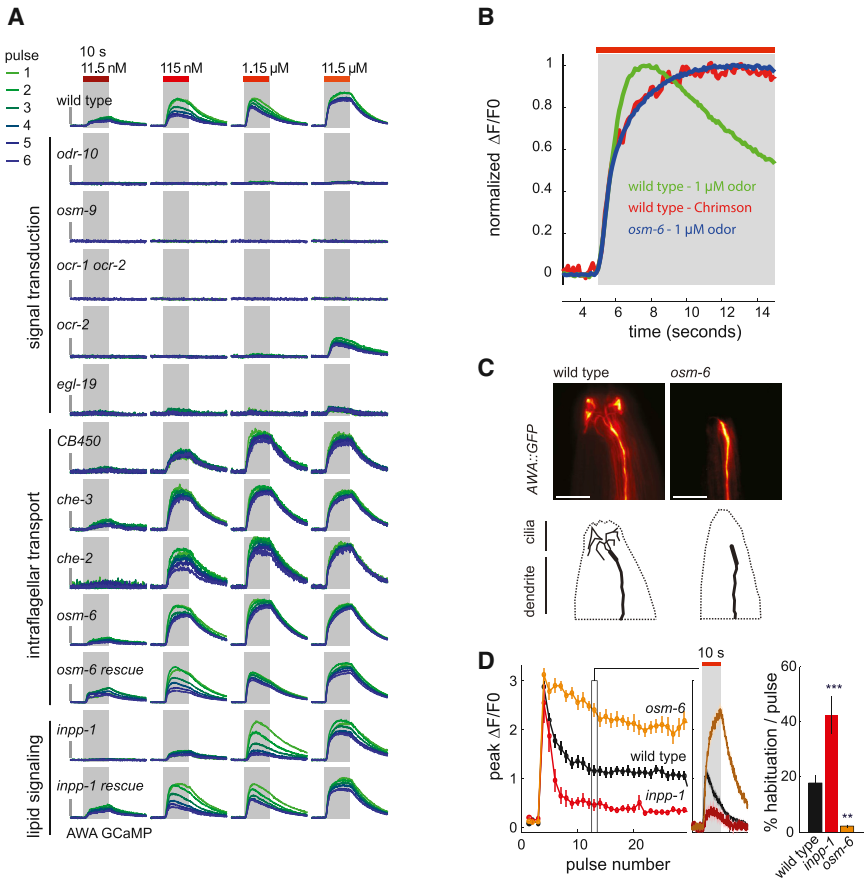

Figure 4. Intraflagellar Transport and Inositol Lipids Modulate AWA Responses

(A) AWA calcium response during odor stimulation in olfactory signal transduction mutants, IFT mutants, and *inpp-1(ky121)* mutants. Gray vertical bars indicate 1 ΔF/F0. Note that these are 10-s pulses, not 30-s pulses as in Figure 2. See also Figures S2 and S3.

(B) AWA calcium dynamics in wild-type and IFT mutants. AWA calcium responses to 1.15 µM diacetyl or Chrimson (11 mW/cm^2), normalized to peak calcium. Rapid desensitization to odor is not observed in Chrimson and *osm-6;* accelerated time-to-peak is driven by rapid desensitization (Figure 3).

(C) Fluorescence z stack projection of anterior tip of representative animals expressing GFP in AWA sensory neurons showing sensory dendrite and cilia. Scale bar, 10 µm.

(D) Peak AWA calcium response and habituation rate for 10-s pulses of 1.15 µM diacetyl delivered once every 60 s. Traces in the center show AWA response during the tenth odor pulse.

Error bars and shading represent SEM. n = 5–12 animals per genotype. **p < 0.01, ***p < 0.001 versus wild-type.

responses to diacetyl at low concentrations, and habituated more quickly upon repeated stimulation than wild-type (Figures 4A and 4D); they were also defective in sensory responses mediated by a second neuron, ASH (Figure S4). Linkage analysis and whole-genome sequencing mapped this defect to a missense mutation in the predicted phosphoinositol-5-phosphatase (INPP5) encoded by T25B9.10, *inpp-1*. Two additional *inpp-1* loss-of-function mutants had similar AWA calcium defects (Figure S3). The sensory defect in AWA was rescued either by a genomic fosmid clone covering *inpp-1,* or by AWA-specific expression of cDNAs encoding either of two tested protein isoforms of T25B9.10 (Figures 4A and S3). Thus, *inpp-1* acts within AWA to regulate odor responses.

A GFP-tagged INPP-1 protein was widely expressed in neurons and distributed through the cytoplasm (Figure S4). AWA neurons in *inpp-1(ky121)* mutants appeared normal, with characteristic branched cilia. However, the expression of ODR-10 diacetyl receptors in AWA cilia was subtly altered in *inpp-1* mutant animals, suggesting a possible alteration in receptor localization or cilia structure (Figure S4).

The AIA Interneurons Respond to Diacetyl Downstream of AWA and Other Sensory Neurons

To determine how AWA activation is relayed to its synaptic targets, we began with the AIA interneurons that affected diacetyl chemotaxis in microfluidic gradients. AIA calcium responses are largely restricted to the neurites (Chalasani et al., 2010), which responded to diacetyl pulses from 1 nM to 100 µM with transient calcium increases (Figure 5A). AIA responses to 1–10 nM diacetyl were graded and sustained across a 10-s odor pulse, whereas responses at higher concentrations peaked within 1–3 s of odor onset and then desensitized (Figure 5A). The AIA response in this range was stereotyped in its magnitude and dynamics, varying little between concentrations or across trials (Figures 5A and S5). These results suggest that diacetyl responses in AIA are highly sensitive, saturating, and relatively uniform with respect to odor concentration over a 100-fold range.

A panel of mutants was used to identify the sensory origin of AIA diacetyl responses. In *odr-10(ky32)* AWA diacetyl receptor mutants and in *odr-7(ky4)* mutants defective in AWA development, AIA responses to diacetyl were reduced in magnitude and delayed in onset compared to wild-type animals (Figures 5A–5C). Thus, AWA is responsible for the fast response in AIA, but other sensory neurons also play a role. A possible source of the residual response is the AWC neurons, which support diacetyl chemotaxis at high concentrations (Chou et al., 2001). A *ceh-36(ky646)* mutation that affects the development of AWC and ASEL sensory neurons (Lanjuin et al., 2003) had near-normal AIA calcium responses to diacetyl, but *ceh-36(ky646) odr-7(ky4)* double-mutant animals lacked almost all responses, suggesting that the second sensory neuron that senses diacetyl could be AWC or ASEL (Figures 5A–5C).

The synaptic connection between AWA and AIA was probed directly by expressing the red-shifted channelrhodopsin derivative Chrimson in AWA neurons and expressing GCaMP in AIA to record calcium signals. This experiment should minimize contributions of AWC, ASEL, and other unknown sensory neurons to

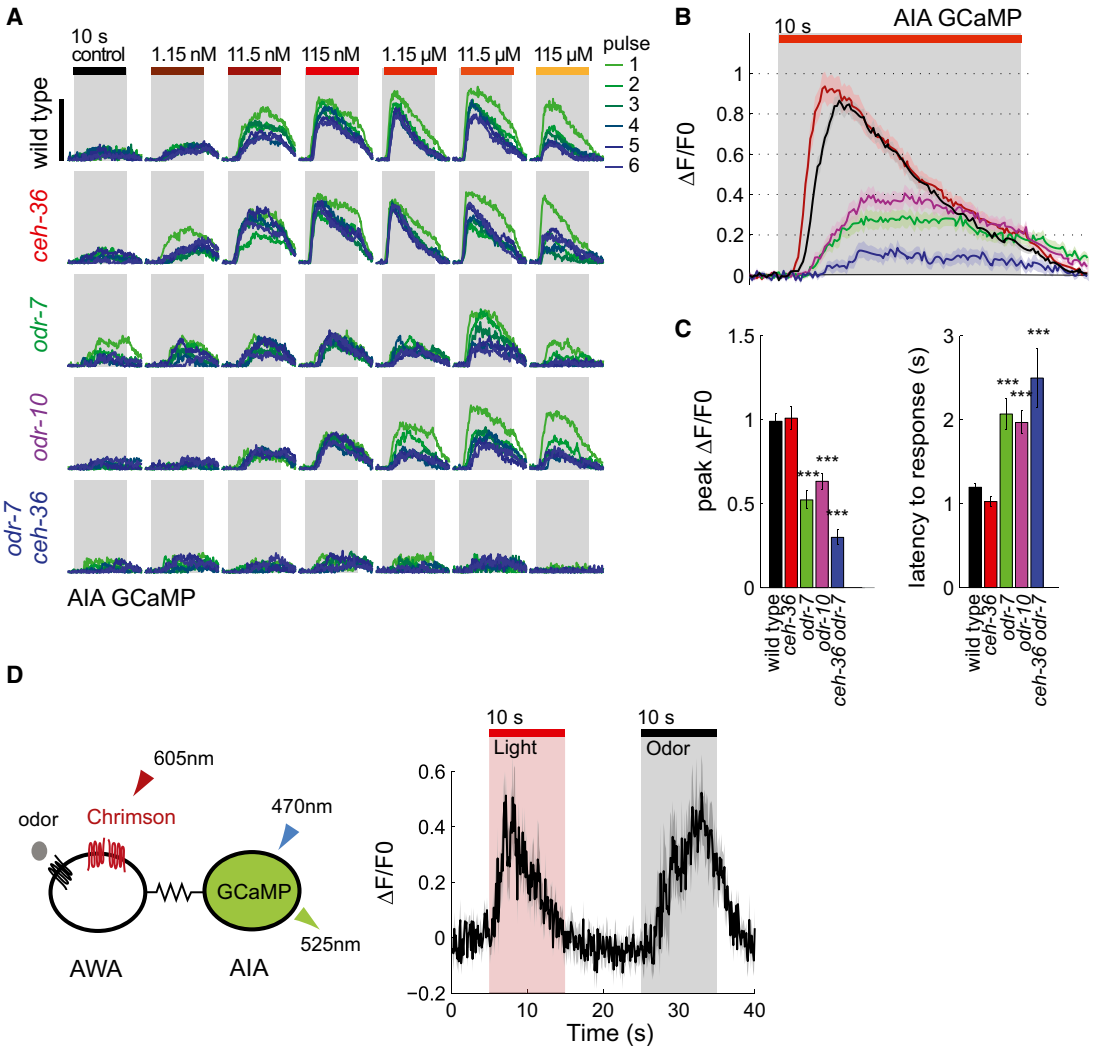

Figure 5. AIA Integrates Diacetyl Inputs from AWA and Other Sensory Neurons

(A) AIA neurite calcium response to 10-s pulses of diacetyl, six pulses at each concentration, and n = 9–24 animals per genotype. Black bar indicates 1 ΔF/F0. AIA neurons express GCaMP5(D380Y). *ceh-36(ky640)* disrupts AWC and ASEL cell fate (Lanjuin et al., 2003). *odr-7(ky4)* disrupts AWA cell fate (Sengupta et al., 1994).

(B) AIA neurite calcium response in different genotypes during 10-s pulses of 1.15 µM diacetyl; shading represents SEM. n = 9–24 animals per genotype. Color legend of genotypes matches (A) and (C).

(C) Peak AIA neurite calcium response (left) and latency to response (right) during 10-s pulses of 1.15 µM diacetyl. Latency is defined as time from start of odor pulse until fluorescence levels exceed 2 SDs of baseline fluorescence. Error bars represent SEM. **p < 0.01, ***p < 0.001 versus wild-type.

(D) AWA to AIA signaling. (Left) Expression of the red-shifted Chrimson cation channel in AWA and GCaMP5(D380Y) in AIA. Red light excites Chrimson to depolarize AWA; blue light excites GCaMP5. (Right) AIA neurite calcium response to 10 s Chrimson stimulation of AWA (10 mW/cm^2) alternated with a 10-s pulse of 11.5 nM diacetyl. Note that this odor concentration induces a slowly rising AIA response compared to higher concentrations (A). Shading represents SEM. n = 15 animals.

AIA activation (Figure 5D). Chrimson excitation of AWA induced desensitizing AIA calcium transients that resembled those induced by high odor concentrations, indicating that AWA depolarization is sufficient to drive the characteristic short-lived AIA calcium response (Figure 5D).

AWA and AIA Respond to Fold-Change Increases in Odor Concentration

In natural environments, diffusion and convection can generate many odor patterns, but most experimental studies of olfaction use only sharp odor steps. To model graded odor stimuli, we examined AWA and AIA responses to smaller changes resembling those that animals experience in the sigmoidal odor gradient. A sustained 11.5-nM or 115-nM diacetyl stimulus was delivered for 10 min to define a baseline. Without removing the odor, increasing amounts of diacetyl at a fixed ratio were delivered at one step each minute, with each step representing a 14%, 58%, or 115% increase over the preceding step (a fold-change step; Shoval et al., 2010) (Figures 6A and 6B). The protocol spanned a range of diacetyl concentrations and

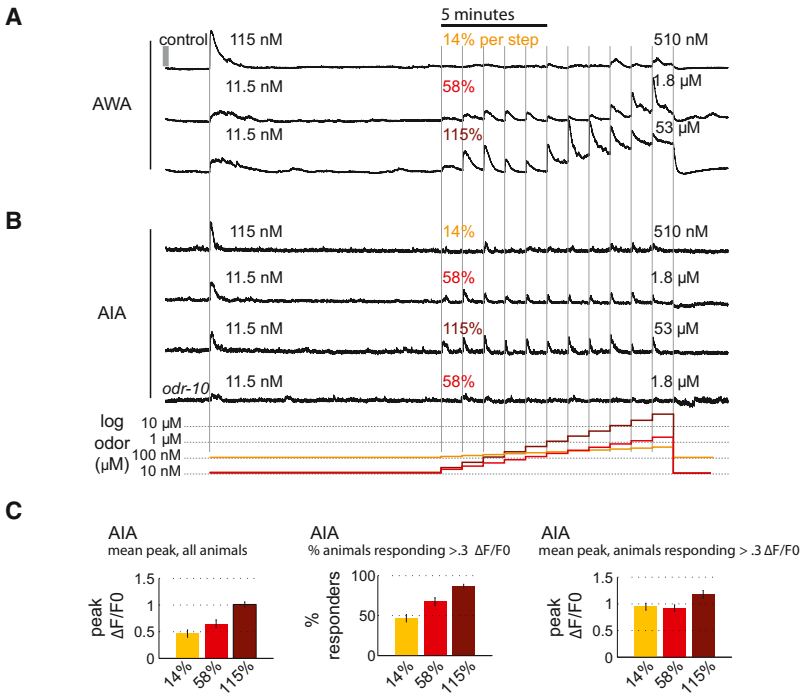

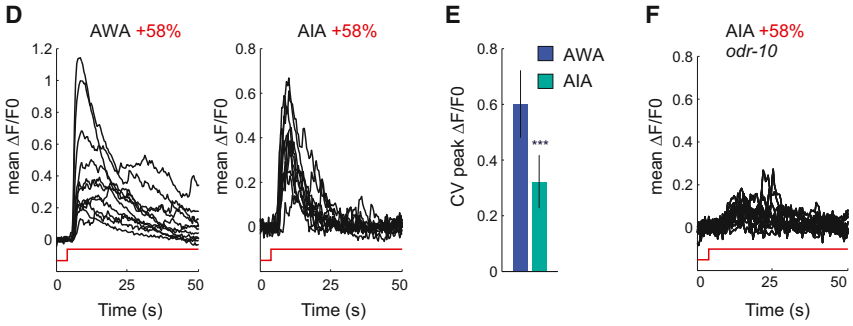

Figure 6. AIA Normalizes AWA Responses to Small Diacetyl Increases

(A and B) AWA calcium response (A) or AIA neurite calcium response (B) during 11 successive fold-change increases in odor concentration. Gray vertical bar indicates 1 ΔF/F0. Odor increase was 14%, 58%, and 115% per step, starting from 115 nM, 11.5 nM, and 11.5 nM, respectively. Legend at bottom illustrates odor concentration at each step.

(C) Larger odor steps from (B) increase the mean AIA response (left panel) and the probability of a response to each upstep (middle panel) but do not greatly increase the peak response magnitude (right panel).

(D) Mean AWA and AIA calcium responses to each 58% fold-change increase, superimposed at the same gain. Note higher variability in AWA calcium response across concentrations. n = 14–16 animals per step.

(E) Coefficient of variation of AWA and AIA calcium responses during 58% fold-change increase. Error bars represent SEM. n = 14–16 animals; ***$p < 0.001$ versus AWA.

(F) AIA neurons in *odr-10* mutants do not respond to 58% fold-change diacetyl increases (n = 10 animals).

concentration changes at which AWA drives chemotaxis behavior (Figure 1B; see Supplemental Experimental Procedures for detailed comparisons of odor concentrations in behavioral and imaging assays).

When presented with a 14% increase in diacetyl concentration, AWA responded weakly (Figure 6A), but when presented with a 58% or 115% step, AWA responded to each diacetyl increase with a calcium increase (Figure 6A). AWA responses desensitized fully within the 60-s pulse at low concentrations but did not desensitize fully at concentrations above 500 nM. Even though the AWA response peaked by ~3 µM, desensitization allowed continued detection of increases above this level. This response provides a potential explanation for the strong desensitization of AWA calcium responses near 1 µM: desensitization allows AWA to respond to diacetyl increases instead of saturating.

AIA interneurons responded to fold-change odor increases with calcium transients that desensitized fully within each pulse (Figure 6B). The fraction of responding AIA neurons changed with the size of the concentration change, such that each animal responded to less than half of the 14% odor steps but to most 58% steps and 115% steps (Figure 6C). In contrast with AWA, AIA responses to fold-change increases were stereotyped in magnitude and dynamics, regardless of the absolute diacetyl concentration (Figure 6D). Accordingly, AIA had a 2-fold lower coefficient of variation than AWA for peak response magnitudes across the tested odor concentrations (Figure 6E). The normalized responses in AIA appeared to report odor increases more accurately than odor concentrations.

AIA responses to diacetyl fold-change increases required the AWA diacetyl receptor ODR-10 (Figures 6B and 6F), even at concentrations at which AIA could have responded to larger diacetyl steps without AWA or ODR-10 input (Figure 5). Thus, AWA is essential for the transmission of fold-change increases to AIA.

AWA and AIA had asymmetric calcium responses to odor increases and decreases. Neither AWA nor AIA responded significantly to small decreases; large decreases (53 µM to 10 nM diacetyl) resulted in a large fall in AWA calcium, with no detectable change in AIA (Figures 6A and 6B). Thus, AWA and AIA are elements of a circuit module that preferentially detects small increases over decreases in odor concentrations.

AWA and AIA Suppress Turning upon Small Increases in Odor Concentrations

In the biased random-walk mechanism of chemotaxis, turning rates are suppressed when attractive odors increase and enhanced when they decrease. In agreement with this model,

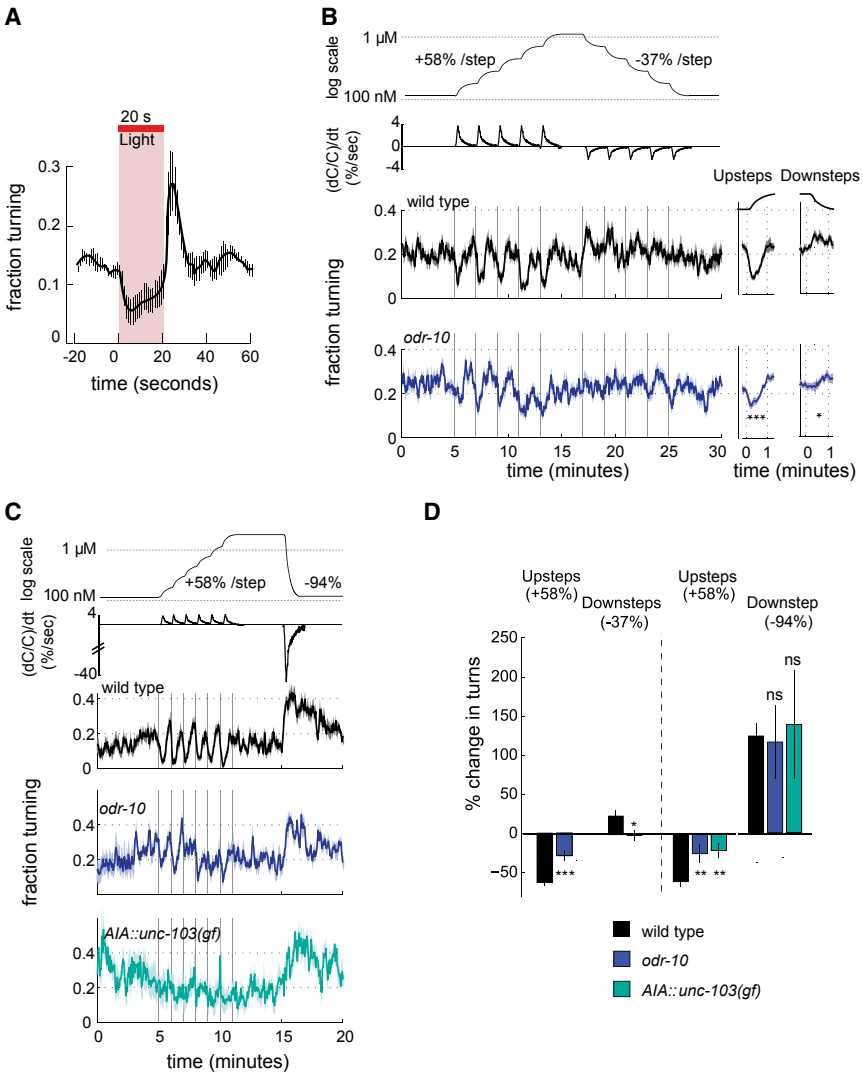

Figure 7. AWA and AIA Drive Behavioral Responses to Small Diacetyl Increases

(A) Behavior of animals expressing Chrimson in AWA during and after 20 s of light stimulation. Animals were filmed as they moved freely on agar plates, and instantaneous turning frequencies (encompassing reversals and omega turns) were scored automatically in 1-s time bins. Error bars represent SEM. n = 3 experiments with 15–20 animals each.

(B) Behavioral responses of freely moving animals to fold-change odor increases and decreases, delivered once per minute in microfluidic arenas. Odor concentrations (shown on log scale) and the change in relative odor concentration over time, (dC/C)/dt, are shown at top; fold-changes result in a constant (dC/C)/dt. Instantaneous fraction of wild-type and *odr-10* animals turning during the diacetyl stimulation protocol is shown at bottom. At right, average response over all fold-change steps. A 58% increase corresponds to a 37% decrease per step. Shading represents SEM. n = 8 assays with 20–30 animals per genotype, two repeats per assay. ***, different from wild-type at $p < 0.001$; *, different from wild-type at $p < 0.05$.

(C) Behavioral responses of freely moving animals to 58% fold-change odor increases and a large 94% step decrease. Odor concentrations and dC/dt are shown at top. Data show instantaneous fraction of animals turning during the diacetyl stimulation protocol. n = 4–10 assays with 20–30 animals per genotype.

(D) Suppression of turning during 58% upsteps and enhancement during large but not small downsteps in experiments in (B) and (C). Bars represent the average change in peak response over all fold-change increases or decreases. Error bars represent SEM. *$p < 0.05$; **$p < 0.01$; ***$p < 0.001$ compared to wild-type; ns, not significant.

direct depolarization of AWA with Chrimson suppressed spontaneous turning within 5 s, and turning off the light after 20 s elicited ~10 s of rebound turning (Figure 7A). To ask how fold-change detection by AWA and AIA relates to behavioral functions, we challenged freely moving animals with fold-change odor upsteps and downsteps in a microfluidic pulse device (Albrecht and Bargmann, 2011) (Figure 7B). Animals were first pre-adapted to 115 nM diacetyl, then exposed to 58% upsteps at 2-min intervals to a final concentration of 1–2 μM. In wild-type animals each odor fold-change upstep caused a transient suppression of turning, with a minimum at 22 ± 5.5 s and a return to baseline over the next 40 s (Figures 7B and 7C). The magnitude and dynamics of suppression were similar for each step. Fold-change increases were poorly detected by animals mutant for the AWA diacetyl receptor ODR-10 (Figures 7B–7D) or by animals with silenced *AIA::unc-103(gf)* interneurons (Figures 7C and 7D), indicating that AWA and AIA mediate the behavioral response.

In contrast with increases, small decreases in diacetyl concentration across the same concentration range had only a small effect on turning rates (Figures 7B and 7D). A large odor downstep from 1.82 μM to 115 nM diacetyl increased turning in wild-type, but also in *odr-10* and *AIA:unc-103(gf)* animals (Figures 7C and 7D). The response to a large downstep thus involves a separate circuit. It may be initiated by AWC neurons, which detect both odor increases and odor decreases, regulate turning bidirectionally, and contribute to diacetyl chemotaxis (Chalasani et al., 2007; Albrecht and Bargmann, 2011; Chou et al., 2001). In summary, the AWA-AIA circuit drives behavioral responses to small fold-change steps whose odor sensitivity, asymmetric preference for increases, and magnitude scaling resemble AIA calcium responses.

DISCUSSION

Sensory circuits across species and modalities have common features that suggest the existence of core circuit motifs and computations. Certain inputs are segregated by polarity; in the retinas of vertebrates and flies, parallel circuits process light onset and light offset (Joesch et al., 2010; Wässle, 2004), and in the olfactory system of *C. elegans*, parallel circuits detect

odor addition and removal (Chalasani et al., 2007). Certain inputs are normalized to maintain specificity; at the first olfactory relay of flies and zebrafish, the response to odor quality is maintained across concentrations by inhibitory neurons that normalize activity to total stimulus level (Carandini and Heeger, 2011; Olsen et al., 2010; Zhu et al., 2013). The circuit including the AWA sensory neurons and AIA interneurons represents a dynamic motif that extracts a particular feature of the stimulus, an increase in concentration over time. The circuit's stereotyped, asymmetric response to fold-change odor increases is distinct from the detection of discrete odor pulses, another dynamic computation in olfaction (Fujiwara et al., 2014; Geffen et al., 2009). Above its apparent threshold, the AIA response is only slightly influenced by the magnitude of change or the ambient odor level. At a behavioral level, AIA is required for an asymmetrical turning motif in which small increases in odor concentration transiently suppress turning. The match between AIA calcium responses, AIA-dependent behaviors, and chemotaxis models provides an algorithm for climbing odor gradients, which could be sought in other olfactory systems as well.

Desensitization in AWA Requires Ciliary Transport

AWA calcium responses desensitize and habituate at the odor concentrations at which AWA is required for chemotaxis. Rapid desensitization endows AWA with the ability to respond repeatedly to successive small increases in odor concentration and to detect changes over a wide range of stimulus intensities without saturation. Desensitization is reduced at very high diacetyl concentrations, which may explain previous observations that AWA is less effective at guiding chemotaxis to high diacetyl than AWC, a less sensitive neuron (Chou et al., 2001). Desensitization may also enable processes such as novelty detection, acute protection from overstimulation, or sharpening of response dynamics for efficient downstream processing (Wark et al., 2007). Interestingly, desensitization is observed in other *C. elegans* sensory neurons whose calcium levels increase with stimulation, like AWA, but is less prominent in sensory neurons whose calcium levels decrease with stimulation, like AWC (Chalasani et al., 2007; Hilliard et al., 2005; Suzuki et al., 2008; Wakabayashi et al., 2009). The depolarizing regime of sensory processing may preferentially encode stimulus change over stimulus level and may help explain why AWA and AWC, which detect similar and even overlapping attractive odors, have distinct sensory transduction properties.

Calcium is only one facet of a neuron's activity, and therefore this view of desensitization is necessarily incomplete. Neuronal calcium is more closely related to the neuronal output than input, and its dynamics are slow; the time resolution of the signal measured here is limited to ~1–2 s and likely underestimates the real speed and complexity of AWA signaling (Neher, 1995; Hires et al., 2008; Figure S1). More precise temporal information awaits electrophysiological studies of AWA odor responses. Nonetheless, AWA desensitization to odor is observed using different sensors and conditions, is always strongest at intermediate odor concentrations around 1 μM, and closely resembles the response to a voltage decrease, suggesting that it is a robust phenomenon reflecting intrinsic AWA activity. Perhaps most importantly, calcium desensitization made the unexpected prediction that AWA would preferentially report odor increases over decreases, a prediction borne out in behavioral experiments.

Desensitization and rapid habituation in the AWA neurons require ciliary genes for IFT. Primary odor responses in AWA did not require IFT proteins, a notable result because most sensory neurons are much less sensitive in IFT mutants, in keeping with their structurally abnormal cilia (Inglis et al., 2007). Although the relatively insensitive GCaMP2.2b indicators would not detect all responses, it is nonetheless evident that IFT mutations affect desensitization mechanisms in AWA more strongly than they affect odor detection. Desensitization may require specific proteins that are normally transported to AWA cilia by IFT, or it may depend more generally upon normal cilia morphology. More speculatively, desensitization could result from acute IFT-dependent translocation of signaling molecules in AWA cilia. The IFT speed of ~0.4 μm/s would easily support movement of molecules through the ~5-μM-long AWA cilia branches, and acute translocation has precedent in *Drosophila* photoreceptors, where several molecules including the TRPL channel are translocated through sensory microvilli during light adaptation (Bähner et al., 2002). The AWA TRPV channel encoded by *osm-9* and *ocr-2* undergoes IFT-dependent transport in other ciliated neurons (Qin et al., 2005), so these channels are candidates for active regulation by IFT.

Regardless of the exact mechanism, the requirement for IFT suggests that AWA desensitization involves the cilia, the site of GPCR signaling. Candidates for regulation include the ODR-10 receptor itself or G protein regulators such as RGS proteins (Krzyzanowski et al., 2013), in addition to TRPV channels. An early site of desensitization, upstream of the essential voltage-activated calcium channel *egl-19*, is also consistent with the weak desensitization when AWA is directly depolarized with Chrimson.

inpp-1 mutants had accelerated habituation to diacetyl, suggesting that inositol phospholipids regulate AWA dynamics. Inositol phospholipids regulate the TRPV channel family (Lukacs et al., 2007), as well as membrane traffic and particularly endocytosis (Di Paolo and De Camilli, 2006), which might relate to the subtle changes in ODR-10 localization observed in mutants. The closest human homolog of *inpp-1* affects the stability of primary cilia, and mutations in this gene can cause Joubert syndrome, a ciliopathy affecting midbrain development (Bielas et al., 2009; Jacoby et al., 2009).

AIA Interneurons Are Specialized to Detect Small Odor Increases

The AIA interneurons compressed the richness of AWA dynamics across diacetyl concentration and history into calcium signals with stereotyped magnitudes and dynamics. Although the normalized AIA response appears to discard information about absolute odor levels that are represented in AWA, additional information can be transmitted to other AWA synaptic partners (Figure 1) to allow multiple computations.

AWA and AIA neurons are connected only by gap junctions in the *C. elegans* wiring diagram, suggesting that they communicate via electrical synapses. The calcium response in AIA is an indirect and delayed representation of activity but can nonetheless provide some information about the relationship between

these neurons. For example, the rapid desensitization of AIA calcium compared to AWA is consistent with three possibilities: shunting of AWA voltage upstream of the gap junction, which seems unlikely as *C. elegans* neurons are believed to be isopotential (Goodman et al., 1998), filtering of AWA signals or active regulation by the gap junctions (Bloomfield and Völgyi, 2009), or intrinsically desensitizing dynamics in AIA.

The AIA response can be understood in the context of the biased random-walk model for *C. elegans* chemotaxis: the model's dependence on dC/dt, rather than absolute odor concentration, is most effectively implemented by concentration-dependent adaptation in the chemotaxis circuit. Adaptation serves as an effective solution for maintaining response sensitivity over a wide input range, a dilemma sometimes called the "sensitivity paradox" in *E. coli* chemotaxis (Sourjik, 2004). The asymmetry, amplification, and stereotypy of the AWA-AIA connection create a possible solution for the sensitivity paradox. Through these processes, small changes in diacetyl concentrations are preferentially sensed and acted upon when diacetyl concentrations rise, a result reminiscent of the bacterial chemotaxis strategy, where turning is suppressed by small increases in attractant concentration but unchanged by small decreases (Berg and Brown, 1972). In both *E. coli* chemotaxis and *C. elegans* diacetyl chemotaxis, sufficiently large decreases in attractants stimulate turning, so the asymmetry is not absolute. It is instructive to compare these results to *C. elegans* salt chemotaxis behavior, where turning rates are symmetrically regulated by concentration increases and decreases (Kunitomo et al., 2013; Luo et al., 2014). The problem solved during salt chemotaxis does not invoke the sensitivity paradox, as the 4-fold (25–100 mM) salt concentration range of this behavior does not require the extreme adaptation required over a 10^5-fold range of diacetyl concentrations.

The sensitivity paradox also applies to the vertebrate visual system, where rod or cone photoreceptor pathways can each maintain sensitivity over 10^6-fold variations in luminance. Like adaptation to diacetyl, adaptation to ambient luminance involves both desensitization within receptor cells and adaptation in downstream bipolar-amacrine cell circuits (Dunn et al., 2007; Ke et al., 2014). However, the logic and details of the systems differ. The most sensitive adaptation in the retina is in downstream circuits (Dunn et al., 2007), whereas the most sensitive adaptation to diacetyl occurs in the AWA sensory neurons. Therefore, while luminance adaptation in the retina, diacetyl adaptation in AWA and AIA, and intracellular adaptation in bacterial chemotaxis perform functionally related computations, they are executed by different mechanisms.

AIA neurons suppress turning when AWA detects diacetyl increases and also suppress spontaneous turning induced by AWC olfactory neurons and ASK gustatory neurons (Chalasani et al., 2007). More complex roles for AIA include integrating positive and negative chemical cues in ambiguous environments and providing neuropeptide feedback to AWC for odor adaptation (Chalasani et al., 2010; Shinkai et al., 2011). These individual examples share some features; for example, the net effect of AIA activity in each case decreases turning. However, the overall effect of the AIA interneuron is determined by the circuit context in which it appears, and as a result AIA can even seem to have opposite valences—AIA enhances chemotaxis initiated by AWA by suppressing turning but inhibits chemotaxis initiated by AWC by a negative feedback loop. These results highlight the importance of understanding neural circuits in the context of the computations they perform, considering their relationship to sensory inputs, distinct motor outputs, and the way that behaviors play out over time.

EXPERIMENTAL PROCEDURES

Standard genetic and molecular biology techniques were used. See Table S1 for a complete strain list.

Stimulus Preparation and Delivery

Odor dilutions were prepared fresh on the day of the experiment from pure stock solutions (2,3-butanedione (diacetyl); Sigma-Aldrich, product 11038). Dilutions for calcium imaging were made in S-basal buffer containing 1 mM acetylcholine agonist (−)-tetramisole hydrochloride (Sigma-Aldrich, product L9756) to paralyze body wall muscles and keep animals stationary. Dilutions for behavioral analysis were made in S-basal buffer.

During dose response experiments, 10-s or 30-s odor pulses were delivered every 60 s at a given concentration, with an additional delay of 60 s between different odor concentrations in ascending order, unless otherwise noted.

Calcium Imaging and Data Analysis

Methods followed those described previously (Larsch et al., 2013). In brief, GCaMP fluorescence was recorded in custom-made microfluidic polydimethylsiloxane (PDMS) chambers allowing parallel observation of ~20 animals during odor stimulation. Continuous liquid flow through the device and over the animals allowed for rapid exchange of chemical stimuli in less than 1 s. In experiments in which Chrimson was activated during calcium imaging, we mounted an external red light-emitting diode above the imaging chamber and used an excitation filter to narrow illumination to a 605 ± 25 nM band. Tiff stack movies were acquired on an Andor iXon3 DU-897 EM-CCD or a Hammamatsu Orca Flash 4 sCMOS camera at 10 fps. Neuron fluorescence was analyzed using custom scripts written for ImageJ (Neurotracker), and MATLAB was used for subsequent data analysis and display. Most statistical comparisons were made by ANOVA using the Bonferroni correction for multiple comparisons. Additional details are provided in the Supplemental Experimental Procedures.

Electrophysiology

AWA neurons were recorded using single-electrode whole-cell current clamp largely as described (Goodman et al., 1998; Liu et al., 2009). An animal was glued to a glass coverslip and a small incision was used to expose the AWA neuron, which was identified by expression of an mCherry reporter.

Supplemental Experimental Procedures includes the identification of *che-3(ky1018)* and *inpp-1(ky121)*, scoring of cilia in *inpp-1(ky121)*, and detailed descriptions of microfluidic behavioral assays (odor gradients, odor pulses), comparisons between different microfluidic assays, calcium imaging and analysis, electrophysiology recording conditions, and molecular biology.

SUPPLEMENTAL INFORMATION

Supplemental Information includes Supplemental Experimental Procedures, five figures, one table, and one movie and can be found with this article online at http://dx.doi.org/10.1016/j.celrep.2015.08.032.

AUTHOR CONTRIBUTIONS

J.L. designed, performed, and interpreted behavioral, genetic, and imaging experiments and co-wrote the paper. Q.L. performed electrophysiology experiments, S.W.F. developed molecular tools, A.G. contributed to analytical methods, and D.R.A. developed microfluidic arenas for behavior and imaging. C.I.B. designed and interpreted experiments and co-wrote the paper.

ACKNOWLEDGMENTS

We thank Christine Cho, Donovan Ventimiglia, Jamal Rahi, and May Dobosiewicz for discussions and comments on the manuscript, Marlis Denk-Lobnig for analyzing *arr-1* mutants, Alison North at the Rockefeller Bio-Imaging Resource Center for assistance acquiring confocal images, and the Rockefeller University Genomics Resource Center for whole-genome sequencing. Some strains were provided by the CGC, which is funded by NIH Office of Research Infrastructure Programs (P40 OD010440). J.L. was supported by a fellowship from the Boehringer Ingelheim Fonds. D.R.A. is supported by a Burroughs Wellcome Career Award at the Scientific Interface. C.I.B. is an Investigator of the Howard Hughes Medical Institute (HHMI). This work was supported by the HHMI.

Received: April 1, 2015
Revised: July 20, 2015
Accepted: August 7, 2015
Published: September 10, 2015

REFERENCES

Akerboom, J., Chen, T.-W., Wardill, T.J., Tian, L., Marvin, J.S., Mutlu, S., Calderón, N.C., Esposti, F., Borghuis, B.G., Sun, X.R., et al. (2012). Optimization of a GCaMP calcium indicator for neural activity imaging. J. Neurosci. *32*, 13819–13840.

Albrecht, D.R., and Bargmann, C.I. (2011). High-content behavioral analysis of *Caenorhabditis elegans* in precise spatiotemporal chemical environments. Nat. Methods *8*, 599–605.

Atema, J. (1995). Chemical signals in the marine environment: dispersal, detection, and temporal signal analysis. Proc. Natl. Acad. Sci. USA *92*, 62–66.

Bähner, M., Frechter, S., Da Silva, N., Minke, B., Paulsen, R., and Huber, A. (2002). Light-regulated subcellular translocation of *Drosophila* TRPL channels induces long-term adaptation and modifies the light-induced current. Neuron *34*, 83–93.

Bargmann, C.I. (2006). Comparative chemosensation from receptors to ecology. Nature *444*, 295–301.

Bargmann, C.I., Hartwieg, E., and Horvitz, H.R. (1993). Odorant-selective genes and neurons mediate olfaction in *C. elegans*. Cell *74*, 515–527.

Benhamou, S., and Bovet, P. (1989). How animals use their environment: a new look at kinesis. Anim. Behav. *38*, 375–383.

Berg, H.C., and Brown, D.A. (1972). Chemotaxis in *Escherichia coli* analysed by three-dimensional tracking. Nature *239*, 500–504.

Bielas, S.L., Silhavy, J.L., Brancati, F., Kisseleva, M.V., Al-Gazali, L., Sztriha, L., Bayoumi, R.A., Zaki, M.S., Abdel-Aleem, A., Rosti, R.O., et al. (2009). Mutations in INPP5E, encoding inositol polyphosphate-5-phosphatase E, link phosphatidyl inositol signaling to the ciliopathies. Nat. Genet. *41*, 1032–1036.

Bloomfield, S.A., and Völgyi, B. (2009). The diverse functional roles and regulation of neuronal gap junctions in the retina. Nat. Rev. Neurosci. *10*, 495–506.

Carandini, M., and Heeger, D.J. (2011). Normalization as a canonical neural computation. Nat. Rev. Neurosci. *13*, 51–62.

Chalasani, S.H., Chronis, N., Tsunozaki, M., Gray, J.M., Ramot, D., Goodman, M.B., and Bargmann, C.I. (2007). Dissecting a circuit for olfactory behaviour in *Caenorhabditis elegans*. Nature *450*, 63–70.

Chalasani, S.H., Kato, S., Albrecht, D.R., Nakagawa, T., Abbott, L.F., and Bargmann, C.I. (2010). Neuropeptide feedback modifies odor-evoked dynamics in *Caenorhabditis elegans* olfactory neurons. Nat. Neurosci. *13*, 615–621.

Chou, J.H., Bargmann, C.I., and Sengupta, P. (2001). The *Caenorhabditis elegans odr-2* gene encodes a novel Ly-6-related protein required for olfaction. Genetics *157*, 211–224.

Di Paolo, G., and De Camilli, P. (2006). Phosphoinositides in cell regulation and membrane dynamics. Nature *443*, 651–657.

Dunn, F.A., Lankheet, M.J., and Rieke, F. (2007). Light adaptation in cone vision involves switching between receptor and post-receptor sites. Nature *449*, 603–606.

Franz, M.O., and Mallot, H.A. (2000). Biomimetic robot navigation. Robot. Auton. Syst. *30*, 133–153.

Fujiwara, T., Kazawa, T., Sakurai, T., Fukushima, R., Uchino, K., Yamagata, T., Namiki, S., Haupt, S.S., and Kanzaki, R. (2014). Odorant concentration differentiator for intermittent olfactory signals. J. Neurosci. *34*, 16581–16593.

Geffen, M.N., Broome, B.M., Laurent, G., and Meister, M. (2009). Neural encoding of rapidly fluctuating odors. Neuron *61*, 570–586.

Goodman, M.B., Hall, D.H., Avery, L., and Lockery, S.R. (1998). Active currents regulate sensitivity and dynamic range in *C. elegans* neurons. Neuron *20*, 763–772.

Hilliard, M.A., Apicella, A.J., Kerr, R., Suzuki, H., Bazzicalupo, P., and Schafer, W.R. (2005). In vivo imaging of *C. elegans* ASH neurons: cellular response and adaptation to chemical repellents. EMBO J. *24*, 63–72.

Hires, S.A., Tian, L., and Looger, L.L. (2008). Reporting neural activity with genetically encoded calcium indicators. Brain Cell Biol. *36*, 69–86.

Iino, Y., and Yoshida, K. (2009). Parallel use of two behavioral mechanisms for chemotaxis in *Caenorhabditis elegans*. J. Neurosci. *29*, 5370–5380.

Inglis, P.N., Ou, G., Leroux, M.R., and Scholey, J.M. (2007). The sensory cilia of *Caenorhabditis elegans* (March 8, 2007). *WormBook*, ed. The *C. elegans* Research Community, http://dx.doi.org/10.1895/wormbook.1.126.2, http://www.wormbook.org.

Izquierdo, E.J., and Lockery, S.R. (2010). Evolution and analysis of minimal neural circuits for klinotaxis in *Caenorhabditis elegans*. J. Neurosci. *30*, 12908–12917.

Jacoby, M., Cox, J.J., Gayral, S., Hampshire, D.J., Ayub, M., Blockmans, M., Pernot, E., Kisseleva, M.V., Compère, P., Schiffmann, S.N., et al. (2009). INPP5E mutations cause primary cilium signaling defects, ciliary instability and ciliopathies in human and mouse. Nat. Genet. *41*, 1027–1031.

Joesch, M., Schnell, B., Raghu, S.V., Reiff, D.F., and Borst, A. (2010). ON and OFF pathways in *Drosophila* motion vision. Nature *468*, 300–304.

Kato, S., Xu, Y., Cho, C.E., Abbott, L.F., and Bargmann, C.I. (2014). Temporal responses of *C. elegans* chemosensory neurons are preserved in behavioral dynamics. Neuron *81*, 616–628.

Ke, J.-B., Wang, Y.V., Borghuis, B.G., Cembrowski, M.S., Riecke, H., Kath, W.L., Demb, J.B., and Singer, J.H. (2014). Adaptation to background light enables contrast coding at rod bipolar cell synapses. Neuron *81*, 388–401.

Klapoetke, N.C., Murata, Y., Kim, S.S., Pulver, S.R., Birdsey-Benson, A., Cho, Y.K., Morimoto, T.K., Chuong, A.S., Carpenter, E.J., Tian, Z., et al. (2014). Independent optical excitation of distinct neural populations. Nat. Methods *11*, 338–346.

Krzyzanowski, M.C., Brueggemann, C., Ezak, M.J., Wood, J.F., Michaels, K.L., Jackson, C.A., Juang, B.T., Collins, K.D., Yu, M.C., L'etoile, N.D., and Ferkey, D.M. (2013). The C. elegans cGMP-dependent protein kinase EGL-4 regulates nociceptive behavioral sensitivity. PLoS Genet. *9*, e1003619. http://dx.doi.org/10.1371/journal.pgen.1003619.

Kunitomo, H., Sato, H., Iwata, R., Satoh, Y., Ohno, H., Yamada, K., and Iino, Y. (2013). Concentration memory-dependent synaptic plasticity of a taste circuit regulates salt concentration chemotaxis in *Caenorhabditis elegans*. Nat. Commun. *4*, 2210. http://dx.doi.org/10.1038/ncomms3210.

Lanjuin, A., VanHoven, M.K., Bargmann, C.I., Thompson, J.K., and Sengupta, P. (2003). Otx/otd homeobox genes specify distinct sensory neuron identities in *C. elegans*. Dev. Cell *5*, 621–633.

Larsch, J., Ventimiglia, D., Bargmann, C.I., and Albrecht, D.R. (2013). High-throughput imaging of neuronal activity in *Caenorhabditis elegans*. Proc. Natl. Acad. Sci. USA *110*, E4266–E4273. http://dx.doi.org/10.1073/pnas.1318325110.

Liu, Q., Hollopeter, G., and Jorgensen, E.M. (2009). Graded synaptic transmission at the *Caenorhabditis elegans* neuromuscular junction. Proc. Natl. Acad. Sci. USA *106*, 10823–10828.

Lukacs, V., Thyagarajan, B., Varnai, P., Balla, A., Balla, T., and Rohacs, T. (2007). Dual regulation of TRPV1 by phosphoinositides. J. Neurosci. *27*, 7070–7080.

Luo, L., Wen, Q., Ren, J., Hendricks, M., Gershow, M., Qin, Y., Greenwood, J., Soucy, E.R., Klein, M., Smith-Parker, H.K., et al. (2014). Dynamic encoding of perception, memory, and movement in a *C. elegans* chemotaxis circuit. Neuron *82*, 1115–1128.

Matsuura, T., Izumi, J., Hioki, M., Nagaya, H., and Kobayashi, Y. (2013). Sensory interaction between attractant diacetyl and repellent 2-nonanone in the nematode Caenorhabditis elegans. J Exp Zool A Ecol Genet Physiol *319*, 285–295.

Montell, C. (2012). *Drosophila* visual transduction. Trends Neurosci. *35*, 356–363.

Neher, E. (1995). The use of fura-2 for estimating Ca buffers and Ca fluxes. Neuropharmacology *34*, 1423–1442.

Olsen, S.R., Bhandawat, V., and Wilson, R.I. (2010). Divisive normalization in olfactory population codes. Neuron *66*, 287–299.

Petersen, C.I., McFarland, T.R., Stepanovic, S.Z., Yang, P., Reiner, D.J., Hayashi, K., George, A.L., Roden, D.M., Thomas, J.H., and Balser, J.R. (2004). In vivo identification of genes that modify ether-a-go-go-related gene activity in *Caenorhabditis elegans* may also affect human cardiac arrhythmia. Proc. Natl. Acad. Sci. USA *101*, 11773–11778.

Pierce-Shimomura, J.T., Morse, T.M., and Lockery, S.R. (1999). The fundamental role of pirouettes in *Caenorhabditis elegans* chemotaxis. J. Neurosci. *19*, 9557–9569.

Qin, H., Burnette, D.T., Bae, Y.-K., Forscher, P., Barr, M.M., and Rosenbaum, J.L. (2005). Intraflagellar transport is required for the vectorial movement of TRPV channels in the ciliary membrane. Curr. Biol. *15*, 1695–1699.

Reisert, J., and Zhao, H. (2011). Perspectives on: information and coding in mammalian sensory physiology: response kinetics of olfactory receptor neurons and the implications in olfactory coding. J. Gen. Physiol. *138*, 303–310.

Richmond, J.E., Davis, W.S., and Jorgensen, E.M. (1999). UNC-13 is required for synaptic vesicle fusion in *C. elegans*. Nat. Neurosci. *2*, 959–964.

Rieke, F., and Rudd, M.E. (2009). The challenges natural images pose for visual adaptation. Neuron *64*, 605–616.

Riffell, J.A., Abrell, L., and Hildebrand, J.G. (2008). Physical processes and real-time chemical measurement of the insect olfactory environment. J. Chem. Ecol. *34*, 837–853.

Roayaie, K. (1996). Studies of chemosensory signal transduction in *Caenorhabditis elegans*. PhD thesis (San Francisco: The University of California, San Francisco).

Satoh, Y., Sato, H., Kunitomo, H., Fei, X., Hashimoto, K., and Iino, Y. (2014). Regulation of experience-dependent bidirectional chemotaxis by a neural circuit switch in *Caenorhabditis elegans*. J. Neurosci. *34*, 15631–15637.

Sengupta, P., Colbert, H.A., and Bargmann, C.I. (1994). The *C. elegans* gene *odr-7* encodes an olfactory-specific member of the nuclear receptor superfamily. Cell *79*, 971–980.

Sengupta, P., Chou, J.H., and Bargmann, C.I. (1996). *odr-10* encodes a seven transmembrane domain olfactory receptor required for responses to the odorant diacetyl. Cell *84*, 899–909.

Shinkai, Y., Yamamoto, Y., Fujiwara, M., Tabata, T., Murayama, T., Hirotsu, T., Ikeda, D.D., Tsunozaki, M., Iino, Y., Bargmann, C.I., et al. (2011). Behavioral choice between conflicting alternatives is regulated by a receptor guanylyl cyclase, GCY-28, and a receptor tyrosine kinase, SCD-2, in AIA interneurons of *Caenorhabditis elegans*. J. Neurosci. *31*, 3007–3015.

Shoval, O., Goentoro, L., Hart, Y., Mayo, A., Sontag, E., and Alon, U. (2010). Fold-change detection and scalar symmetry of sensory input fields. Proc. Natl. Acad. Sci. USA *107*, 15995–16000.

Sourjik, V. (2004). Receptor clustering and signal processing in *E. coli* chemotaxis. Trends Microbiol. *12*, 569–576.

Suzuki, H., Thiele, T.R., Faumont, S., Ezcurra, M., Lockery, S.R., and Schafer, W.R. (2008). Functional asymmetry in *Caenorhabditis elegans* taste neurons and its computational role in chemotaxis. Nature *454*, 114–117.

Tian, L., Hires, S.A., Mao, T., Huber, D., Chiappe, M.E., Chalasani, S.H., Petreanu, L., Akerboom, J., McKinney, S.A., Schreiter, E.R., et al. (2009). Imaging neural activity in worms, flies and mice with improved GCaMP calcium indicators. Nat. Methods *6*, 875–881.

Vergassola, M., Villermaux, E., and Shraiman, B.I. (2007). 'Infotaxis' as a strategy for searching without gradients. Nature *445*, 406–409.

Wakabayashi, T., Kimura, Y., Ohba, Y., Adachi, R., Satoh, Y., and Shingai, R. (2009). In vivo calcium imaging of OFF-responding ASK chemosensory neurons in *C. elegans*. Biochim. Biophys. Acta *1790*, 765–769.

Wark, B., Lundstrom, B.N., and Fairhall, A. (2007). Sensory adaptation. Curr. Opin. Neurobiol. *17*, 423–429.

Wässle, H. (2004). Parallel processing in the mammalian retina. Nat. Rev. Neurosci. *5*, 747–757.

Weimer, R.M., Richmond, J.E., Davis, W.S., Hadwiger, G., Nonet, M.L., and Jorgensen, E.M. (2003). Defects in synaptic vesicle docking in *unc-18* mutants. Nat. Neurosci. *6*, 1023–1030.

White, J.G., Southgate, E., Thomson, J.N., and Brenner, S. (1986). The structure of the nervous system of the nematode *Caenorhabditis elegans*. Philos. Trans. R. Soc. Lond. B Biol. Sci. *314*, 1–340.

Wicks, S.R., de Vries, C.J., van Luenen, H.G.A.M., and Plasterk, R.H.A. (2000). CHE-3, a cytosolic dynein heavy chain, is required for sensory cilia structure and function in *Caenorhabditis elegans*. Dev. Biol. *221*, 295–307.

Wilson, R.I. (2013). Early olfactory processing in *Drosophila*: mechanisms and principles. Annu. Rev. Neurosci. *36*, 217–241.

Zhu, P., Frank, T., and Friedrich, R.W. (2013). Equalization of odor representations by a network of electrically coupled inhibitory interneurons. Nat. Neurosci. *16*, 1678–1686.

Cell Reports

Supplemental Information

A Circuit for Gradient Climbing in *C. elegans* Chemotaxis

Johannes Larsch, Steven W. Flavell, Qiang Liu, Andrew Gordus, Dirk R. Albrecht, and Cornelia I. Bargmann

Figure S1

A

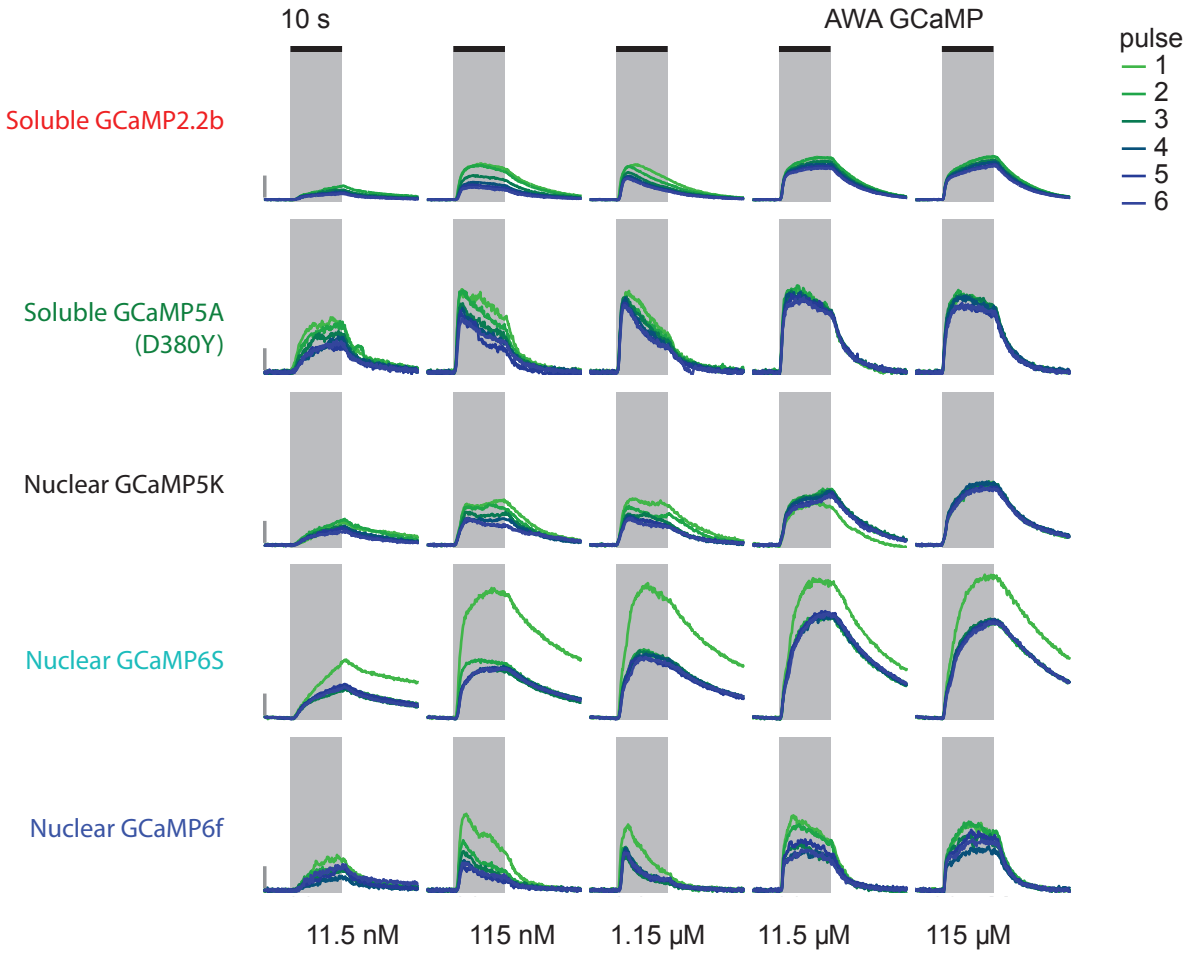

B

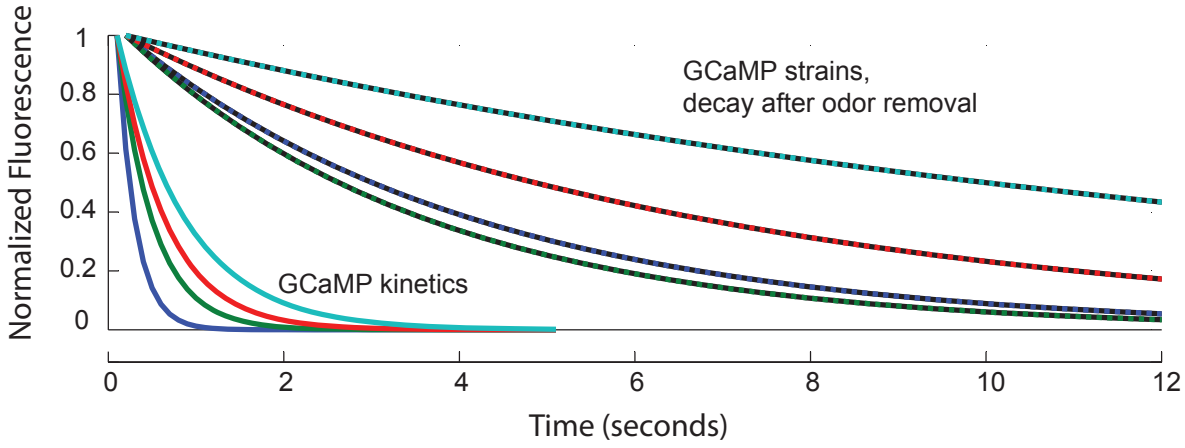

GCaMP kinetics from *in vitro* data

GCaMP	$t_{1/2}$ decay (s)
3(2.2b)	0.38
5a	0.28
6s	0.55
6f	0.14

Strain-specific response dynamics at 1.15 µM odor

	soluble	soluble	nuclear	nuclear
	2.2b	5a	6s	6f
$t_{1/2}$ rise	0.44 s	0.37 s	1.1 s	0.36 s
$t_{1/2}$ odor	6.4 s	6 s	24.7 s	3.5 s
$t_{1/2}$ decay	4.6 s	2.6 s	10 s	2.4 s

Figure S1. Technical considerations of measurements with genetically-encoded calcium indicators, related to Figures 2 and 3.

a) Odor responses in AWA neurons expressing five different calcium indicators, using a series of 10-s odor pulses. No GCaMP indicator showed desensitization at the lowest or highest diacetyl concentration, and all showed significant desensitization at 1.15 µM. In agreement with their published properties, the GCaMP5 and 6 series are more sensitive than GCaMP2.2b, and nuclear GCaMP indicators have slower calcium response than cytoplasmic indicators. Gray vertical bars on the left indicate 1 ΔF/F0.

b) Relationship between GCaMP binding, calcium buffering, and apparent calcium decay. Graph shows the biophysical k_{off} for GCaMP sensors (Tian et al., 2009, Akerboom et al., 2012, Chen et al., 2013; Badura et al., 2014), as well as the experimentally measured decay times for calcium signals after odor removal in strains shown in panel (a) (1.15 µM diacetyl). Table shows half-time of rise, decay in odor, and decay after odor removal.

The fluorescence response of a calcium indicator depends on its sensitivity, ie the Kd for calcium; its cooperativity, which, together with the Kd, determines the calcium level at which the fluorescence signal saturates; its dynamic range, the fluorescence change upon calcium binding; and its intrinsic off-rates coupled with the strain-specific expression level of the calcium indicator, which will determine the fastest signals it can report (Hires et al., 2008). There are tradeoffs among these factors. Typically, the most sensitive indicators such as GCaMP6s saturate at lower calcium levels and have slower dynamics due to a lower k_{off}, faster reporters such as GCaMP6f have a higher Kd and are less sensitive, and high dynamic range reporters have dim baseline fluorescence that makes ratio changes harder to quantify. Previous reports indicate that GCaMP2.2b is comparable in sensitivity to GCaMP3 and GCaMP6f (Kd~350-400 nM), but less sensitive than GCaMP5A (Kd ~300 nM), GCaMP5k (Kd~190 nM), or GCaMP6s (Kd~140 nm)(Tian et al., 2009, Akerboom et al., 2012, Chen et al., 2013). Compared to more recently developed reporters, GCaMP2.2b has a relatively low dynamic range (2.2-fold). In agreement with these results, we observed that GCaMP2.2b had a poor signal-to-noise ratio compared to the other indicators, and did not detect the lowest odor levels.

Nonetheless, the more sensitive GCaMP5A indicator reported the same dynamic properties as the GCaMP2.2b strain, with a desensitization profile that peaked near 1 uM diacetyl and habituation between pulses. Therefore, GCaMP2.2b sensitivity is limiting for detecting signals at threshold, but not limiting for detecting desensitization.

Among additional technical issues, high expression of calcium indicators can silence *C. elegans* neurons (Tian et al., 2009); we observed a slight decrease in diacetyl chemotaxis in GCaMP2.2b animals. Nuclear GCaMP reporters have been reported to be less toxic (Schrodel et al., 2013), so they may provide a less distorted, albeit slower, view of calcium dynamics. We observed desensitization within odor pulses with two nuclear calcium indicators, GCaMP5k and GCaMP6f. The third indicator, GCaMP6s, is very sensitive but a slow reporter of calcium dynamics that only reported desensitization at 1.15 µM odor.

The difference between the biochemical and cellular decay times of GCaMP signals in panel (**b**) is observed in all biological tissues (eg Chen et al., 2013) and results from two factors: the slow efflux of calcium relative to its fast entry, and the calcium buffering activity of the cell and of GCaMP (Neher, 1995; Hires et al., 2008). Decay is described by the formula

$$tau_{observed} = (1 + k_s + k_b)/\gamma$$

where $tau_{observed}$ is the observed decay time, k_s is the intrinsic calcium buffering of the cell, k_b is the calcium buffering produced by the exogenous calcium indicator, and γ is the rate of calcium efflux. For nuclear GCaMPs in *C. elegans* neurons, tau incorporates an additional decay time of ~1 s due to diffusion (Saul Kato, personal communication).

k_b will have a characteristic value for each transgenic strain approximately proportional to the product of the GCaMP k_{off} and the GCaMP expression level. k_b is generally large compared to k_s, and therefore limits the effective tau of decay. This appears to be true of the strains in (b), which express GCaMPs at comparable levels; each strain's decay time is 10-20 times slower than the decay time of the corresponding GCaMP.

Even with a slow $tau_{observed}$, the time at which calcium decay begins can be detected as an immediate change in slope, for example upon odor removal. However, the $tau_{observed}$

limits the ability to distinguish between an instantaneous decrease and a slower process that overlaps tau. The fastest $tau_{observed}$ among these five strains is GCaMP5a (t½ of decay = 2.4 s) followed by nuclear GCaMP6f (t½ of decay = 2.8 s). For practical purposes, this provides a limit to the speed of measurement of calcium decay in each strain; an instantaneous decay is indistinguishable from one that occurs over ~2 s.

The t½ during a calcium increase is not significantly affected by calcium buffering. The effective temporal resolution in the imaging experiments presented here is approximately 0.5 s, and is limited by the flow rate in the microfluidic delivery system. Desensitization that overlaps the rise results in an earlier calcium peak, as observed in odor compared to Chrimson (see Figure 4b).

Figure S2

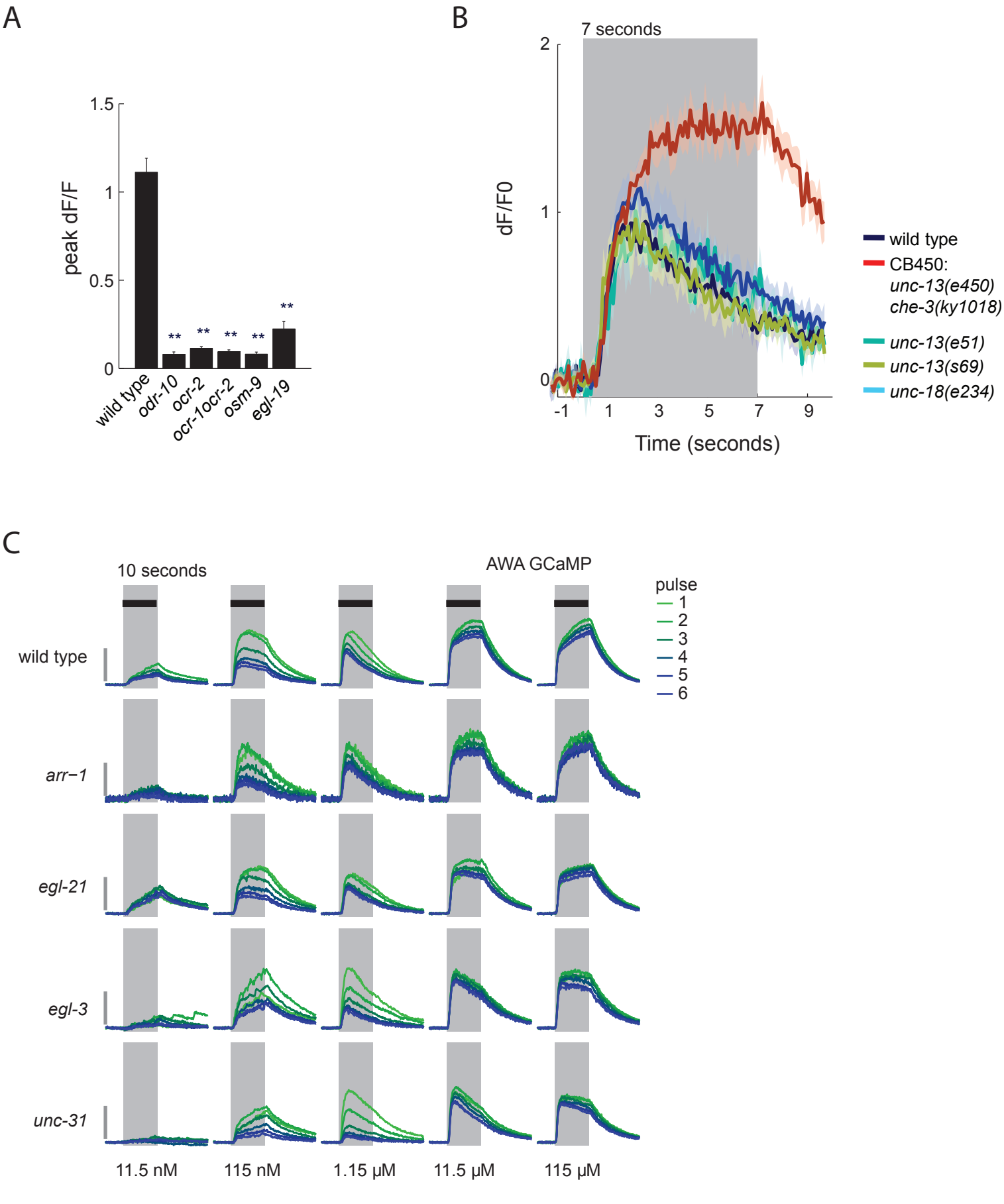
A
peak dF/F
1.5
1
0.5
0
**
wild type
odr-10
ocr-2
ocr-1ocr-2
osm-9
egl-19
B
7 seconds
dF/F0
2
1
0
-1
1
3
5
7
9
Time (seconds)
wild type
CB450:
unc-13(e450)
che-3(ky1018)
unc-13(e51)
unc-13(s69)
unc-18(e234)
C
10 seconds
AWA GCaMP
pulse
1
2
3
4
5
6
wild type
arr−1
egl-21
egl-3
unc-31
11.5 nM
115 nM
1.15 µM
11.5 µM
115 µM

Figure S2. AWA calcium responses to diacetyl in mutant backgrounds, related to Figure 4.

a) Peak calcium response of mutants shown in Figure 4A to 1.15 µM diacetyl. Error bars, s.e.m. **, different from wild-type at P<0.01.

b) Calcium responses of fast synaptic transmission mutants *unc-13* and *unc-18* to 1.15 µM diacetyl. The imaging strain CX14881, derived from CB450, has linked *unc-13* and *che-3* mutations. Shading, s.e.m.

c) Calcium responses of the arrestin mutant *arr-1* and three mutants with abnormal neuropeptide processing or release (Carboxypeptidase E processing enzyme EGL-21, Kex-type proprotein convertase EGL-3, and CAPS dense core vesicle release factor UNC-31).

Figure S3

A

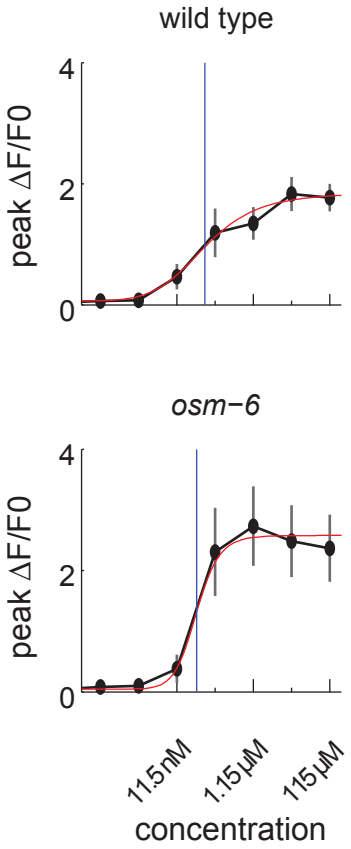

B

	Chrimson	1.15 µM diacetyl						
	WT	WT	*osm-6*	rescue	*che-2*	*che-3*	*inpp-1*	rescue
$t_{1/2}$ rise	1 s	0.6 s	0.7 s	0.5 s	0.6 s	0.9 s	0.7 s	0.6 s
$t_{1/2}$ odor	25 s	7.4 s	na	12 s	na	na	11.7 s	10 s
$t_{1/2}$ decay	5 s	5 s	6 s	6 s	5 s	5 s	6 s	6 s

C

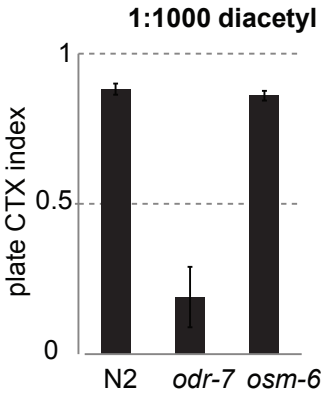

D

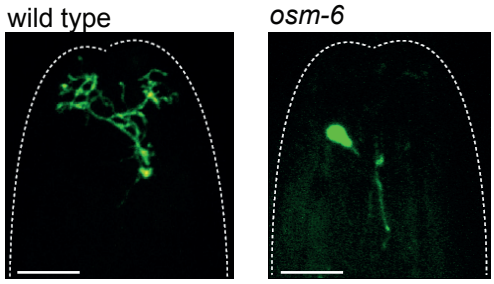

E

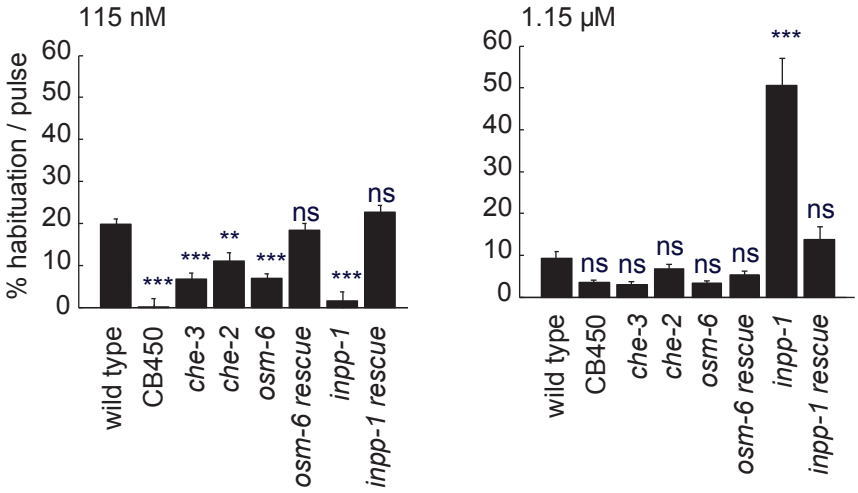

F

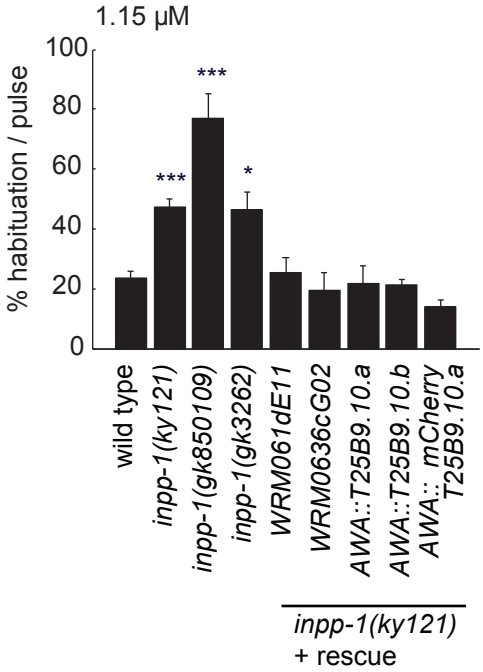

Figure S3. AWA calcium response kinetics in IFT mutants and *inpp-1* mutants, related to Figure 4

a) Dose response curve showing peak AWA calcium response for wild-type and *osm-6* mutants. Error bars represent s.e.m., n=10-21 animals, 6 pulses per concentration).

b) Dynamics of odor responses and Chrimson responses (11 mW/cm^2) in wild-type and mutant strains. Responses in IFT mutants do not decay in sustained odor (na). Decay times after odor removal are indistinguishable.

c) Chemotaxis to a 1:1000 dilution of diacetyl in a standard agar plate assay.

d) Typical image of wild-type and *osm-6* animals expressing ODR-10::GFP in AWA neurons. ODR-10::GFP is localized to the truncated AWA cilia in *osm-6* animals. Scale bar, 10 µm.

e) Reduced habituation in cilium structure mutants and increased habituation in *inpp-1* mutants at 1 µM diacetyl. Note cell-autonomous rescue of *osm-6* and *inpp-1* in AWA.

f) Two *inpp-1* mutants generated by the Million Mutations project (Thompson et al., 2013) have similar habituation defects as *ky121*. The *ky121* mutant defect is rescued by transgenic fosmids (WRM clones) covering the region, or by untagged or mCherry-tagged *inpp-1* cDNAs expressed from an AWA-specific promoter.

In (e) and (f), habituation was induced by ten 10 s pulses of diacetyl delivered once every 60 s. n=7-38 animals per data point. ***P<0.001; **P<0.01, *P<0.05 versus wild type.

Figure S4

A

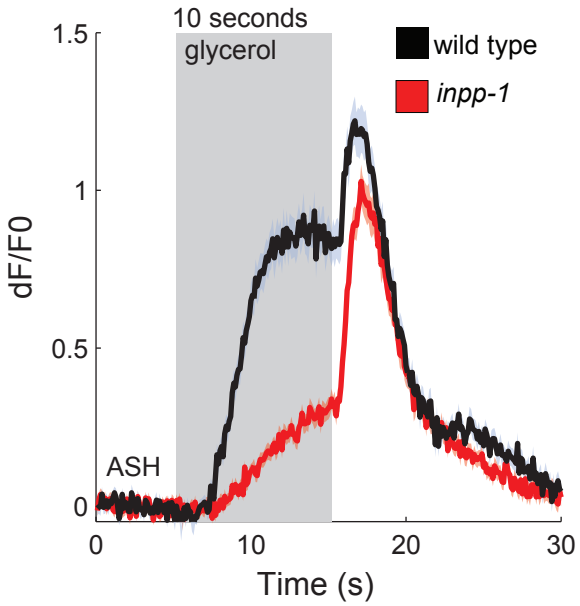

B

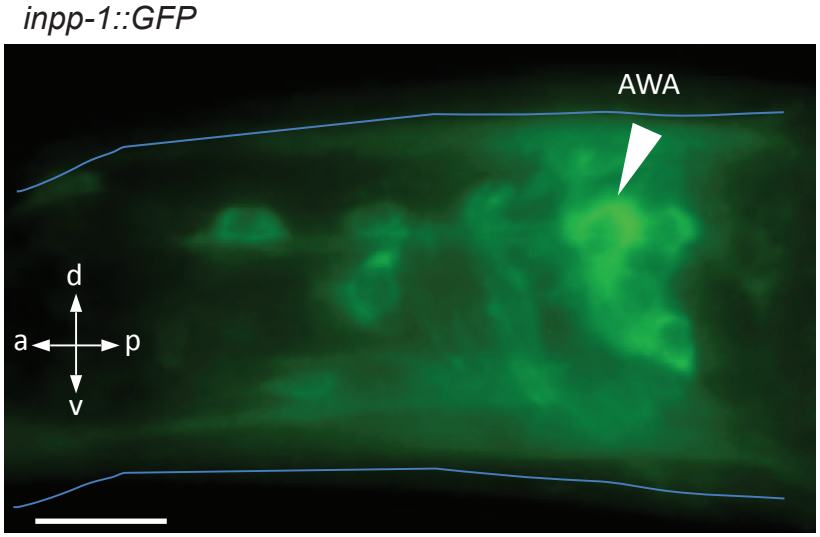

C

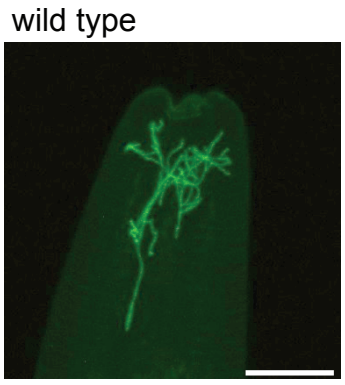

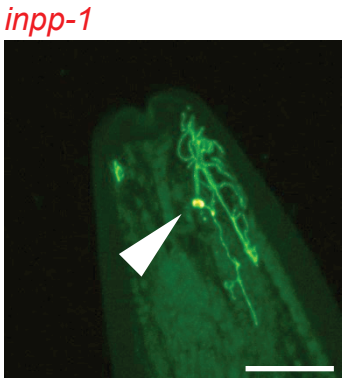

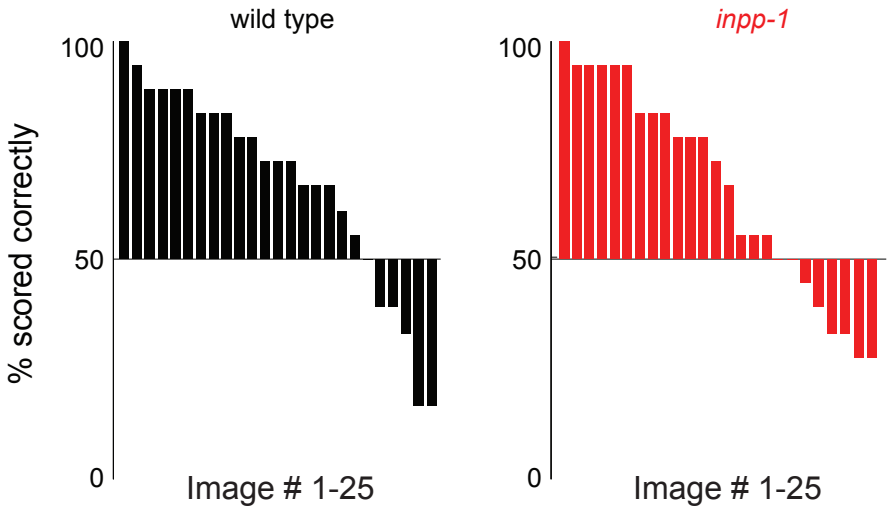

Figure S4. The cytoplasmic neuronal protein INPP-1 affects sensory responses in ASH and the distribution of ODR-10 in AWA cilia, related to Figure 4.

a) Calcium responses of wild-type and *inpp-1* ASH sensory neurons to high osmolarity glycerol, a noxious stimulus. *inpp-1* has a reduced response to glycerol and an enhanced response to glycerol removal. n=9-10 animals per genotype.

b) Translational fusion of full-length INPP-1 protein under its own promoter to GFP. Arrowhead indicates AWA. Scale bar, 10 µm.

c) Typical image of wild-type and *inpp-1* animals expressing ODR-10::GFP in AWA neurons. Arrowhead indicates bright punctum in *inpp-1* mutant. Scale bar, 10 µm.

d), Crowd-sourced scoring of 50 images, 25 each of wild-type (black) and *inpp-1* (red) animals, by 18 volunteers trained on 10 different images (5 wild-type, 5 *inpp-1)*. Each image came from a different animal. Scoring performance of unlabeled images was different from chance for both genotypes ($P<10^{-13}$, 67% scored correct for each genotype, see methods).

Figure S5

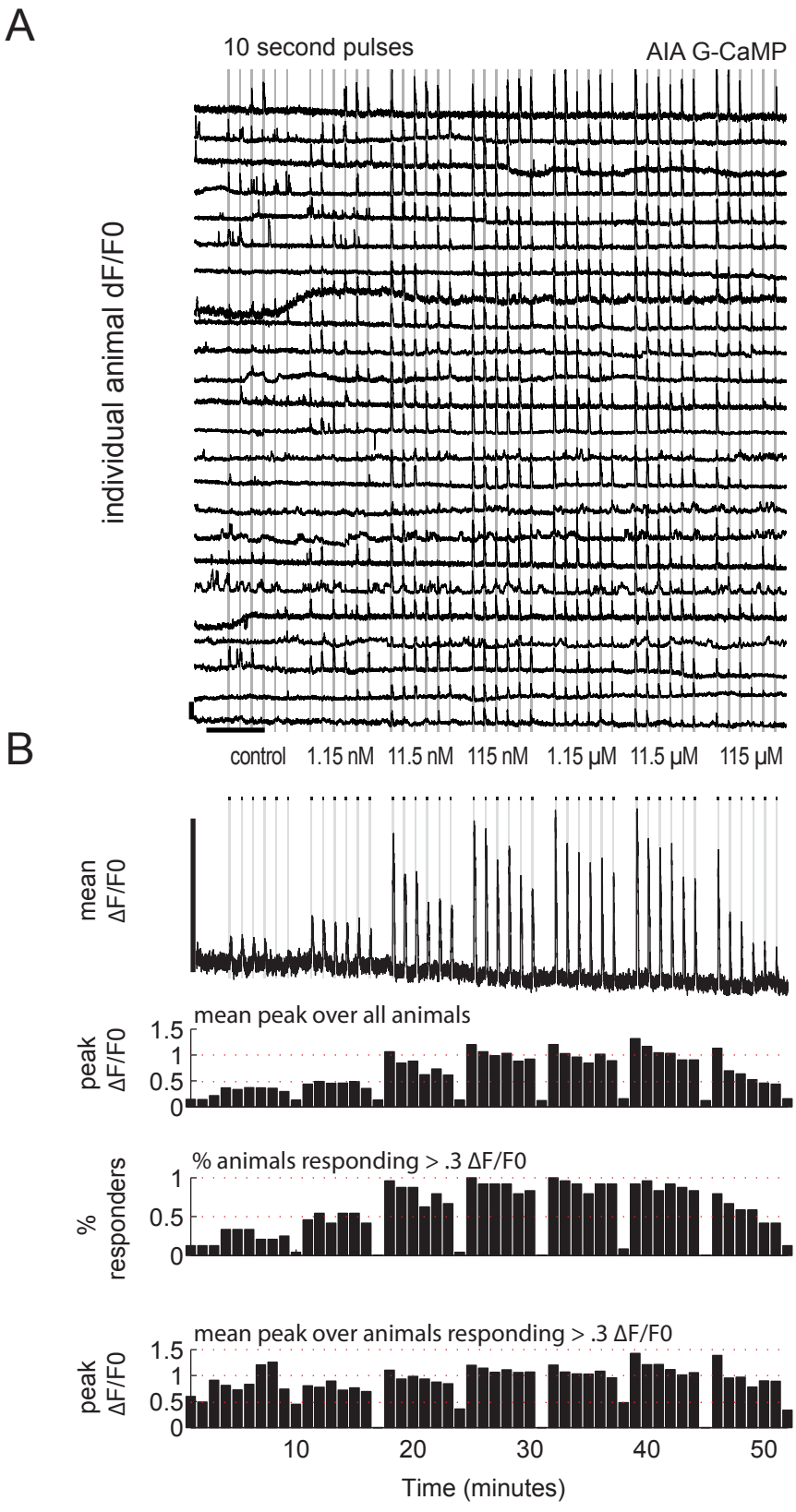
A
10 second pulses
AIA G-CaMP
individual animal dF/F0
control
1.15 nM
11.5 nM
115 nM
1.15 µM
11.5 µM
115 µM
B
mean ΔF/F0
mean peak over all animals
peak ΔF/F0
1.5
1
0.5
0
% animals responding > .3 ΔF/F0
% responders
1
0.5
0
mean peak over animals responding > .3 ΔF/F0
peak ΔF/F0
1.5
1
0.5
0
10
20
30
40
50
Time (minutes)

Figure S5. AIA calcium responses in individual animals, related to Figure 5.

a) AIA neurite fluorescence during dose response experiment; each row represents a single animal. Each diacetyl concentration was presented six times for 10 s separated by 60 s, with an additional 60 s between concentration blocks. Black vertical bar indicates 1 ΔF/F0. Black horizontal bar indicates 5 minutes.

b) AIA response magnitude. Top panel, mean AIA response from traces in (a). Black vertical bar indicates 1 ΔF/F0. Second panel, the mean peak response varies 2-fold with odor concentration. Third panel, the probability of a response increases 2-fold with odor concentration. Bottom panel, the mean peak of responses above a threshold of 0.3 ΔF/F increases <1.5-fold with odor concentration.

Supplemental Movie 1, related to Figure 1. Chemotaxis of wild-type and *odr-10* animals in sigmoidal diacetyl gradients in microfluidic devices, as in Figure 1b. Movie is sped up 60-fold.

Supplemental Table 1, List of strains, related to all Figures.

Strain	Genotype	Figure(s)
CX32	*odr-10(ky32) X*	1, 7
CX14597	*kyEx4745[gcy-28dp::unc-103(gf)*::SL2::*mCherry* 30ng/ul, *elt-2::mCherry* 2ng/ul, pSM 70ng/ul*]*	1, 7
CX14887	*kyIs587[gpa-6p*::*G-CaMP2.2b* 50ng/ul, *unc-122::dsRed* 15ng/ul, pSM 35ng/ul*]* This strain was previously published as *kyIs598* (Larsch et al., 2013).	2, 3, 4, 6, S1-S4
CX11826	*kyEx3208[odr-7::GFP* 15ng/ul + *ofm-1::RFP* 15ng/ul, pSM 70ng/ul*]*	4
CX15804	*osm-6(p811) V; kyEx3208*	4
CX15889	*osm-6(p811) V*	S3
CX3344	*kyIs53[odr-10::gfp]*	S4
CX15892	*inpp-1(ky121) IV; kyIs53*	S4
CX15257	*kyEx5128[gcy28d::GCaMP D380Y* 50ng/ul, *unc-122::dsRed,* pSM 50ng/ul*]*	5, 6, S5
CX16169	*ceh-36(ky640) X; kyEx5128*	5
CX16170	*odr-10(ky32*) *X; kyEx5128*	5
CX16171	*odr-7(ky4) X; kyEx5128*	5
CX15510	*ocr-2(ak47) IV; kyIs587*	4, S2
CX15909	*ocr-2(ak47) IV; ocr-1(ok132) V; kyIs587*	4, S2
CX15614	*osm-9(ky10) IV; kyIs587*	4, S2
CX15127	*odr-10(ky32) X; kyIs587*	4, S2
CX15217	*egl-19(n582) IV*; *kyIs587*	4, S2
CX14881	*unc-13(e450) che-3(ky1018) I; kyIs587* [CB450 crossed to CX14887]	4, S2, S3
CX14882	*unc-18(e234) X; kyIs587*	S2
CX15128	*unc-13(e51) I; kyIs587*	S2
CX15129	*unc-13(s69*) *I; kyIs587*	S2
CX16012	*arr-1(ok401) X; kyIs587*	S2
CX16337	*egl-21(n476) IV; kyIs587*	S2
CX14883	*egl-3(ok979) V; kyIs587*	S2
CX16168	*egl-31(e928) III; kyIs587*	S2
CX15505	*osm-6(p811) V; kyIs587*	4, S3
CX15509	*che-2(e1033) X; kyIs587*	4, S3

CX15545	*che-3(e1124) I; kyIs587*	4, S3
CX15959	*osm-6(p811) V; kyIs587; kyEx5406[odr-7p::mCherry::osm-6* 5ng/ul, *elt-2::mCherry* 2ng/ul, pSM 95ng/ul*]*	4, S3
CX15615	*inpp-1(ky121) IV; kyIs587*	4, S3
CX15793	*inpp-1(gk850109*) *IV; kyIs587*	S3
CX15831	*inpp-1(gk3262) IV; kyIs587*	S3
CX15763	*inpp-1(ky121) IV; kyIs587*; *kyEx5298[*WRM061dE11 2ng/ul, *elt-2::mCherry* 2ng/ul, pSM 96ng/ul*]*	S3
CX15765	*inpp-1(ky121) IV; kyIs587*; *kyEx5300[*WRM0636cG02 2ng/ul, *elt-2::mCherry* 2ng/ul, pSM 96ng/ul*]*	S3
CX15800	*inpp-1(ky121) IV; kyIs587*; *kyEx5325[odr-7p::inpp-1a::sl2::mCherry* 3ng/ul, *elt-2::mCherry 2ng/ul*, pSM 95ng/ul*]*	S3
CX15801	*inpp-1(ky121) IV; kyIs587*; *kyEx5326[odr-7p::inpp-1b::sl2::mCherry* 3ng/ul, *elt-2::mCherry* 2ng/ul, pSM 95ng/ul*]*	4, S3
CX15958	*inpp-1(ky121) IV; kyIs587; kyEx5405[odr-7p::mCherry::inpp-1a* 5ng/ul, elt-*2::mCherry* 2ng/ul, pSM 95ng/ul*]*	S3
CX16082	*kyEx4520[inpp-1::GFP* (TransgeneOmics fosmid clone 39735925444913767 C08) 5ng/ul, *unc-122::dsRed* 15ng/ul, pSM 80ng/ul.]*; kyEx5405[odr-7p::mCherry::inpp-1a* 5ng/ul, *elt-2::mCherry* 2ng/ul, pSM 95ng/ul*]*	S4
CX15304	*kyIs602[p-sra-6:GCaMP3* 75ng/uL, *unc-122:GFP* 10ng/ul*]*	S4
CX15832	*inpp-1(ky121) IV; kyIs602[p-sra-6:GCaMP3* 75ng/uL, *unc-122:GFP* 10ng/ul*]*	S4
CX16561	*kyEx5128; kyEx5662[odr-7p::Chrimson::SL2::mCherry* 5ng/ul, *elt-2::mCherry 2 ng/ul*, pSM 93 ng/ul*]*	5, 7
CX16573	*kyIs587; kyEx5662[odr-7p::Chrimson::SL2::mCherry* 5ng/ul, *elt-2::mCherry* 2 ng/ul, pSM 93 ng/ul*]*	3, 4, S3
CX16152	*kyEx5511[gpa-6::NLS-GCaMP6S::SL2::NLS-mCherry* 30ng/ul, *myo-3::mCherry* 5 ng/ul*]*	S1
CX16216	*kyEx5530[gpa-6::NLS-GCaMP5K* 30ng/ul, *myo-3::mCherry* 5ng/ul]	S1
CX16323	*kyEx5556[gpa-6::NLS-GCaMP6F* 50ng/ul, *myo-3::mCherry* 5ng/ul*]*	S1
CX15130	*kyEx5056[gpa-6p::G-CaMP5 D380Y* 30ng/ul, *elt-2::mCherry* 2ng/ul, *pSM* 70ng/ul*]*	S1
CX4	*odr-7(ky4) X*	S3

Supplemental Experimental Procedures

Nematode Culture

Strains were raised at 20°C on nematode growth medium (NGM) plates, seeded with *Escherichia coli* OP50 bacteria as a food source (Brenner, 1974). Wild-type worms were the Bristol strain N2. All experiments were performed with young adults, age-synchronized by picking L4 stage animals to fresh food plates 12-24 h before the experiment. A complete strain list appears in Supplemental Table 1.

Molecular Biology

To hyperpolarize the AIA neurons, we used a *gcy-28d* promoter to express the ether-a-go-go-related potassium channel UNC-103 (*C30D11.1f* isoform) containing an A331T point mutation that increases channel conductance at voltages below -20 mV (Petersen et al., 2004). We initially used cell-specific promoters to drive the entire genomic region of *unc-103* from *unc-103(n500gf)* animals (Shinkai et al., 2011), but observed unexpected expression suggesting the existence of enhancers within *unc-103* introns. The *unc-103* cDNA was therefore amplified from pooled wild-type cDNA and the A331T mutation associated with the *n500gf* mutant allele introduced by overlap extension PCR. Expression of this cDNA with SL2::GFP bicistronic reporters matched known expression patterns for the promoters of interest.

A Chrimson cDNA with three synthetic introns was generated to match the published amino acid sequence (Klapoetke et al., 2014).

For cell type specific transgene expression, we amplified promoters from N2 genomic lysate using the following primers:

gpa-6: 5’-ttGGCGCGCCttcaaaataacattgaaagtcaatacacc-3’ and
5’-ttGGCGCGCCggcaccgatttcaaaataaca-3’;

odr-7: 5’-ttGGCCGGCCcgtccgagcagcttttattc-3’ and
5’-ttGGCGCGCCctagattttgaaaggaaata-3’;

gcy-28d: 5’-ttGGCCGGCCtacaattgtagtgagcttcg-3’ and
5’-ttGGCGCGCCttcgcactcatctcaccatt-3’

Calcium Imaging

The arena size in the PDMS chips was 3x3 mm or 4.5x4.5 mm, corresponding to the field of view for imaging. The larger arenas were bisected for simultaneous imaging of two separated groups/genotypes of animals exposed to the same odor stimuli. Before recording, animals were transferred in S-basal buffer into the imaging arena and starved for 1 h in the presence of (-)-tetramisole.

To avoid phototoxicity and photobleaching, excitation illumination was pulsed for 10 ms during each 100 ms exposure from a white LED (Sola, Lumencor) passed through a 470/40 excitation filter (Endow GFP filter set, Chroma, part No. 41017). Excitation-filtered illumination intensity was estimated at 105 mW/cm^2 during continuous illumination using a laser power meter (Edmund Optics, part No. 54-018).

Data Acquisition, Analysis, and Statistics

Tiff stack movies were acquired at 2.5x or 5x magnification on an Andor iXon3 DU-897 EM-CCD or a Hammamatsu Orca Flash 4 sCMOS camera at 10 fps. Neuron fluorescence was analyzed using custom scripts written for ImageJ (Neurotracker, (Larsch et al., 2013)). Background-corrected integrated GCaMP fluorescence was collected from a 4x4 pixel ROI centered on the cell body for AWA. A 4x4 pixel ROI centered on the process that did not include cell body fluorescence was used for AIA.

GCaMP fluorescence was divided by the baseline fluorescence (mean of the first 5 s) to obtain the normalized calcium response $\Delta F/F_0$ for each animal and stimulation trial. Traces showing fluorescence during a full experiment over many trials were normalized only once at the beginning. In most cases, a single animal was subjected to multiple odor pulses at a given concentration, and the responses were averaged to obtain a single data point for statistical analysis. Population averages thus report the mean and standard error of averaged individual animal responses unless otherwise noted.

Neuronal calcium responses were categorized as desensitizing if the fluorescence maximum occurred within 10 s of odor application. The maximum was determined by the MATLAB function *max* on fluorescence data smoothed using the MATLAB function *smooth* and a sliding average of 5 frames (0.5 seconds).

Decay constants for desensitizing traces were calculated by fitting individual animal fluorescence data to the exponential decay model $y(t) = c + y_0*\exp(-k*t)$ using the MATLAB curve fitting function *nlinfit*. For desensitization, fluorescence data starting at the time of the fluorescence maximum and ending at stimulus removal was used for the fit. Similarly, rise constants were obtained by fitting the function $1 - \exp(-k*t)$ to normalized fluorescence data from response onset to the time of the fluorescence maximum. Response onset was determined as the time of smoothed fluorescence above 10% of the maximal response level of a given trace.

Throughout the manuscript, we report $t_{1/2} = \log(2)/k$.

For Figure 3D, post odor decay constants were fit on one trace averaged over all animals at each stimulus level due to the lower signal to noise ratio of individual animal traces in this data set.

Habituation rate was calculated by fitting individual animal peak fluorescence during five successive odor pulses at a given odor concentration to the exponential decay model $y(t) = c + y_0*\exp(-k*t)$ using the MATLAB curve fitting function *nlinfit*. The habitation constant k represents the percent decrease of peak AWA fluorescence per pulse.

The coefficient of variance of peak response magnitudes in AWA vs AIA (Figure 6) was calculated for each animal as the standard deviation of peak responses to the 12 increasing stimuli divided by the mean response.

Simultaneous Optogenetic Stimulation and Calcium Imaging (Figure 3, 5)

To activate Chrimson during calcium imaging we mounted an external red LED (Mightex Precision LED Spot Light, 617nm, Part no.: PLS-0617-030-S, output power: 150 mW) above the microfluidic imaging chamber. Illumination wavelength was narrowed to a 605±25 nm band by passing LED illumination through an excitation filter (Chroma, ET605/50x). There was negligible bleed-through from the red LED into the GCaMP recording wavelength of 525±25 nm (<10% of signal to noise ratio). Animals were fed retinal overnight before the experiment.

The 470 nm light used to excite GCaMP was able to activate Chrimson and trigger calcium transients in some animals when delivered at high intensities, and causes phototoxicity with continued stimulation (Larsch et al., 2013). For AWA recording, undesired activation was reduced by strobing the 470 nm light at a 10% duty cycle (10 ms on, 90 ms off) at an intensity of about 10 mW/cm^2 (10% of light power normally used during wide field imaging).

Because of dimmer GCaMP expression in AIA processes compared to AWA cell bodies, we used light intensities of 100 mW/cm^2 to maintain an acceptable signal to noise ratio for GCaMP imaging and could not entirely eliminate cross-activation of Chrimson. As a consequence, we observed strong blue light-induced calcium transients in AIA at the beginning of the calcium imaging experiments (data not shown). These light signals subsided after one minute of blue light exposure, permitting a subsequent analysis of calcium transients in response to red light activation of Chrimson.

Electrophysiology (Figure 3)

An adult animal was immobilized on a Sylgard-coated (Sylgard 184, Dow Corning) glass coverslip by applying a cyanoacrylate adhesive (Vetbond tissue adhesive; 3M) along the dorsal side of the head region (Liu et al., 2009). A puncture in the cuticle away from the head was made to relieve hydrostatic pressure. A small longitudinal incision was then made between two pharyngeal bulbs along the glue line. The cuticle flap was folded back and glued to the coverslip with GLUture Topical Adhesive (Abbott Laboratories) exposing the nerve ring. The preparation was then treated with 1 mg/mL collagenase (type IV; Sigma) for ~10 s. An upright microscope (Axio Examiner; Carl Zeiss, Inc.) equipped with a 40× water immersion lens and 16× eyepieces was used for viewing the preparation. AWA neurons were identified by mCherry expression from the *odr-7::Chrimson::SL2::mCherry* transgene. All experiments were performed with the bath at room temperature using single-electrode whole-cell current clamp (Heka, EPC-10 USB) with two-stage capacitive compensation optimized at rest, and series resistance compensated to 50%. Borosilicate glass pipettes (BF100-58-10; Sutter Instruments) with resistance (Re) = 10–15 MΩ were used as electrodes. The pipette solution was (all concentrations in mM) [K-gluconate 120; KCl 15; MgCl2 5; TES 5; CaCl2 0.25; EGTA

5; Na2ATP 5; NaGTP 0.5; Hepes 10; Sucrose 30] (pH 7.3, osmolarity 320mOsm) and the extracellular solution was [NaCl 140; NaOH 5; KCl 5; CaCl2 2; MgCl2 5; Sucrose 5; Hepes 15; D-Glucose 25] (pH 7.3, osmolarity 330 mOsm). Experiments were controlled using PatchMaster software (Heka). Analog data were filtered at 2 kHz and digitized at 10 kHz. Light pulses were delivered through the objective lens with a SpectraX Lumencor solid-state light source at 36 mW/cm^2. A 30 s light pulse through a 587/25 nm single band bandpass filter was manually switched on by iVision software (BioVision Technologies) during a 45 s continuous recording of membrane potential under current clamp configuration.

Mapping of a *che-3* mutation in CB450 (Figure 4, S2)

Animals from the CB450 *unc-13(e450)* strain did not show desensitization of AWA responses to 10 s pulses of 1.15 µM diacetyl, whereas other *unc-13* alelles did desensitize. To map the unknown mutation underlying the lack of desensitization, we back-crossed CB450 animals to wild type. The resulting F1 progeny were allowed to self-fertilize, yielding F2 progeny of which ¼ had the uncoordinated phenotype caused by *unc-13(e450)*. 80 uncoordinated F2 animals were screened for desensitization by calcium imaging in groups of 10-15 in a device with four arenas that could be recorded sequentially, allowing us to paralyze and pre-adapt up to 50 animals at once for subsequent testing. Each arena was then recorded once. Analysis of raw AWA fluorescence from individual animals identified 79 non-desensitizing animals and one animal with normal desensitization, suggesting that the desensitization mutant is closely linked but not identical to *unc-13*. The desensitizing F2 animal was recovered from the microfluidic device. Its F3 progeny included both desensitizing and non-desensitizing animals. A stable homozygous line of uncoordinated, desensitizing animals was identified by screening the F4 progeny of F3 candidates; this line was inferred to have lost the mutation that affects desensitization.

We prepared genomic DNA from the desensitizing homozygous line and the original CB450 strain and used standard methods for Illumina whole genome sequencing at the Rockefeller High-Throughput Sequencing facility. Sequence reads were aligned using custom written software (McGrath et al., 2011). Comparison of single nucleotide

polymorphisms (SNPs) that differed between the two strains and the reference genome revealed six coding changes to the right of *unc-13* on chromosome I in CB450 that were lost in the back-crossed strain, including a mutation that changed residue 1107 of *che-3* from Q to STOP, *ky1018.* In addition, strains bearing the canonical *che-3(e1124)* allele failed to desensitize. These and subsequent results indicate that *che-3(ky1018)* is the causal mutation for defective desensitization in CB450.

Mapping of *inpp-1(ky121)* (Figure 4, S3, S4)

ky121 was isolated after EMS mutagenesis based on a defect in pyrazine chemotaxis, an odor detected by AWA (Roayaie, 1996). Genetic mapping established linkage to the left of *unc-30* on chromosome IV, and generated a strain in which *unc-30(e191)* was linked to *ky121*. *ky121 unc-30(e191)* was crossed to the AWA imaging transgene *kyIs587*, F1 progeny were identified, and uncoordinated F2 progeny bearing *kyIs587* were tested for AWA responses to odors, revealing increased desensitization and habituation to diacetyl.

ky121 unc-30(e191) was backcrossed two additional times with wild-type animals, and subjected to whole genome sequencing as above. 12 coding changes were identified within a 4 MB region left of *unc-30*, including a mutation that changed residue 339 of T25B9.10a (*inpp-1*) from P to L. Transgenic rescue of the enhanced desensitization phenotype with a fosmid covering T25B9.10, as well as with a T25B9.10 cDNA under an AWA promoter, identified *inpp-1* as the gene responsible for enhanced desensitization and habituation in *ky121*. Two additional alleles of *inpp-1* were obtained from the Million Mutations Project (Thompson et al., 2013), backcrossed twice by *kyIs587*, and tested for odor responses; both had phenotypes similar to those of *ky121.*

Crowd-sourced scoring of an *inpp-1* mutant phenotype (Figure S4)

Initial observations using images captured on a Zeiss Apotome with a 63X ApoChromat objective suggested that *inpp-1(ky121)* mutant animals had a tendency to exhibit patches of high ODR-10::GFP fluorescence in maximum intensity z-stack projections. For quantification, we imaged 30 young adults per genotype on an inverted TCS SP8 laser scanning confocal microscope (Leica) with a 63X HC PL APO objective. Initial computational attempts using intensity histograms did not recover a difference between

genotypes. As an alternative scoring method, we generated an internet page that displayed five representative images each of wild-type and *inpp-1(ky121)* animals expressing ODR-10::GFP labeled with the correct genotype for reference. Below, we showed 50 additional, unlabeled images and visitors to the page were asked to label these images by paying attention to the fluorescent patches. All images had to be labeled as wild type or mutant. A $20 Amazon gift card was promised as a reward to the participant scoring the highest percentage of images correctly. 18 people (friends and family) participated in this blinded analysis. In total, 900 judgments were made, 450 per genotype (25 images x 18 people). 303 (wild type) and 300 (*inpp-1*) judgments were correct. Based on the binomial distribution, the probability of choosing ≥303/450 or 300/450 correct by guessing 50:50 was ~10^{-13}. Binomial analysis was also conducted on each individual image to calculate the probability of obtaining its score by chance. Using the Benjamini Hochburg correction for multiple comparisons, 14/25 wild-type images were scored correctly and 2/25 wild-type images were scored incorrectly at $p<0.05$. Similarly, for *inpp-1* 13/25 images were scored correctly and 0/25 images were scored incorrectly significantly at $p<0.05$, i.e. most participants scored most images correctly.

Microfluidic gradient assay for behavior (Figure 1, Supplemental Movie 1)

This assay allows each animal to determine its own odor experience by its movement through a well-defined odor gradient. We used microfluidic gradient chambers to create mirror symmetric sigmoidal odor gradients of 32 mm width. Each half of the concentration profile can be approximated by the logistic function $1/(1+\exp(-k*(y-y_0)))$ for $0 < y < 16$ mm, $y_0=8$ mm and $k=0.625$ mm^{-1}. The odor distribution is approximately linear over ~8 mm on the two flanks of the gradient (Figure 1b)(Albrecht and Bargmann, 2011). The device geometry constrains animals to paths parallel to the gradient or at 60° angles relative to the gradient.

We transferred groups of ~20 animals into buffer-filled devices and allowed them to disperse and adapt to the novel environment. After one hour, we started the flow of two different odor concentrations into the device to establish a gradient. One stimulus (A) flowed through the center of the arena and the other stimulus (B) flowed on both sides. A mixing tree upstream of the arena facilitated diffusion between the two stimuli,

generating a smooth gradient of intermediate concentrations. Computer-controlled dynamic switching was used to change the stimulus concentration in the center of the device. Movie S1 shows wild-type and *odr-10* animals in this device.

Animals were video recorded for *post hoc* automated tracking of each animal in the device (Albrecht and Bargmann, 2011). For each experiment, we calculated a chemotaxis index representing the mean distance of all animals from the device center during 2 s time bins (continuous scale from -1 at device edge to +1 at device center).

Microfluidic pulse assay for behavior (Figure 7)

In the pulse assay, all animals in a microfluidic arena are subjected to a defined stimulus change when a computer controlled valve switches between alternative flows into the arena. Each pulse increases the odor concentration as an exponential function with a time constant k of ~20 s. The time constant k reflects diffusive mixing of successive stimuli in the delivery channels before they enter the arena and can be tuned by modulating the flow rate through the device to modify dC/dt. To increase time resolution of the post-hoc analysis of turning behavior in response to odor steps, the timing of odor encounter was corrected for each animal's location in the device based on dye measurements at the same flow rate (Albrecht and Bargmann, 2011).

The range of dC/dt during step pulses was chosen to match the magnitude of dC/dt experienced during gradient crawling (see below).

Comparison of odor concentrations and dC/dt across assays

Odor gradients in nature can form by diffusion from a point source on a substrate. The shape of a diffusing gradient can be described by a Gaussian function that scales with peak odor concentration (Berg, 1993). An animal approaching this gradient from a distance first experiences a nearly exponential rise in odor concentration followed by a more linear regime and finally a shallow increase towards the peak.

In the microfluidic gradient device, we created sigmoidal odor gradients, recapitulating these features (Figure 1b). We chose the edge concentration of 0.115 nM diacetyl near or below the apparent behavioral detection threshold and varied peak gradient

concentrations from 1.15 nM to 115 µM. Animals traversing this gradient at 0.2 mm/s on paths of 60° angles relative to the gradient experienced a relative change in concentration of up to 60% per mm or ~12% per second near the foot of the gradient and gradually weaker relative changes as they approached the peak (Figure 1b). The absolute change in odor concentration experienced across the 8 mm wide linear part of the gradient ranged from 0.028 nM/s – 2.8 µM/s (gradient peak 1.15 nM – 115 µM, respectively).

Animals moving freely in spatial gradients can display the full range of odor triggered chemotaxis behaviors, but it is difficult to disentangle acute odor responses from odor history in this configuration. Acute odor responses are more easily analyzed using odor pulses as stimuli.

The pulse stimuli used in calcium imaging experiments (Figure 6) were designed to mimic the odor changes experienced by an animal during chemotaxis in sigmoidal gradients (Figure 1). To this end we devised a stimulation series consisting of consecutive upsteps in odor concentration at fixed ratios of 14%, 58% or 115% per step. With this protocol, absolute odor concentrations rise exponentially with each step, as they do near the foot of sigmoidal odor gradients. The complete ranges were 115 nM – 510 nM (14% step), 12 nM – 1.8 µM (58% step), or 12 nM – 53 µM (115% step), overlapping the 10 nM – 1 µM range over which AWA is essential for diacetyl chemotaxis in the gradient assay.

In addition to controlling absolute final odor concentration at each step, measurement of dye flow through the different types of microfluidic pulse devices allowed us to quantify switching times and to estimate relative rates of change in odor concentration over time. In the microfluidic device for calcium imaging, odor concentrations switch within ~ 1 second (Figure 2b). The resulting relative rates of change of 14% - 115% per second are at the upper end of what is experienced in the sigmoidal gradient.

The pulse stimuli for behavioral analysis (Figure 7) were also designed to resemble the odors experienced in sigmoidal gradients (Figure 1). For example, in Figure 7d the diacetyl series started with a step from 0.115 to 0.182 µM and ended at 1.82 µM. The dC/dt experienced by the animal ranged from 5 - 50 nM/s (peak dC/dt, Figure 7a), compared with 25 nM/s in the microfluidic gradient assay from 0.1 nM-1.15 µM in

Figure 1b,c. In the microfluidic pulse device for behavioral analysis, odor concentrations switch within ~ 40 seconds (Figure 7a). The resulting relative rates of up to 4%/s are within the middle range experienced in the sigmoidal gradient.

Supplemental References

Badura, A., Sun, X.R., Giovannucci, A., Lynch, L.A., and Wang, S.S.-H. (2014). Fast calcium sensor proteins for monitoring neural activity. Neurophotonics 1, 025008.

Berg, H.C. (1993). Random walks in biology (Princeton, N.J: Princeton University Press).

Brenner, S. (1974). The genetics of *Caenorhabditis elegans*. Genetics *77*, 71–94.

McGrath, P.T., Xu, Y., Ailion, M., Garrison, J.L., Butcher, R.A., and Bargmann, C.I. (2011). Parallel evolution of domesticated *Caenorhabditis* species targets pheromone receptor genes. Nature *477*, 321–325.

Schrödel, T., Prevedel, R., Aumayr, K., Zimmer, M., and Vaziri, A. (2013). Brain-wide 3D imaging of neuronal activity in *Caenorhabditis elegans* with sculpted light. Nat. Methods 10, 1013–1020.

Thompson, O., Edgley, M., Strasbourger, P., Flibotte, S., Ewing, B., Adair, R., Au, V., Chaudhry, I., Fernando, L., Hutter, H., et al. (2013). The million mutation project: a new approach to genetics in *Caenorhabditis elegans*. Genome Res. 23, 1749–1762.